

The XXL Survey[★]

IV. Mass-temperature relation of the bright cluster sample

M. Lieu¹, G. P. Smith¹, P. A. Giles², F. Ziparo¹, B. J. Maughan², J. Démoclès¹, F. Pacaud³, M. Pierre⁴, C. Adami⁵, Y. M. Bahé^{6,7}, N. Clerc⁸, L. Chiappetti¹⁰, D. Eckert^{9,10}, S. Ettori^{11,12}, S. Lavoie¹³, J. P. Le Fevre¹⁴, I. G. McCarthy¹⁵, M. Kilbinger⁴, T. J. Ponman¹, T. Sadibekova⁴, J. P. Willis⁷.

¹ School of Physics and Astronomy, University of Birmingham, Edgbaston, Birmingham, B15 2TT, England
e-mail: mlieu@star.sr.bham.ac.uk

² H. H. Wills Physics Laboratory, University of Bristol, Tyndall Avenue, Bristol, BS8 1TL, England

³ Argelander Institut für Astronomie, Universität Bonn, D-53121 Bonn, Germany

⁴ Service d'Astrophysique AIM, CEA Saclay, F-91191 Gif sur Yvette, France

⁵ Université Aix Marseille, CNRS, LAM (Laboratoire d'Astrophysique de Marseille) UMR 7326, F-13388, Marseille, France

⁶ Max-Planck-Institut für Astrophysik, Karl-Schwarzschild Str. 1, D-85748 Garching, Germany

⁷ Institute of Astronomy, University of Cambridge, Madingley Road, Cambridge CB3 0HA, UK

⁸ Max Planck Institut für Extraterrestrische Physik, Postfach 1312, D-85741 Garching bei München, Germany

⁹ Department of Astronomy, University of Geneva, ch. d'Ecogia 16, 1290 Versoix, Switzerland

¹⁰ INAF - IASF-Milano, Via E. Bassini 15, I-20133 Milano, Italy

¹¹ INAF - Osservatorio Astronomico di Bologna, Via Ranzani 1, I-40127 Bologna, Italy

¹² INFN, Sezione di Bologna, viale Berti Pichat 6\2, I-40127 Bologna, Italy

¹³ Department of Physics and Astronomy, University of Victoria, 3800 Finnerty Road, Victoria, BC, V8P 1A1, Canada

¹⁴ SEDI CEA Saclay, France

¹⁵ Astrophysics Research Institute, Liverpool John Moores University, IC2, 146 Brownlow Hill, Liverpool L3 5RF, UK

Astronomy & Astrophysics, status

ABSTRACT

Context. The XXL survey is the largest survey carried out by *XMM-Newton*. Covering an area of 50 deg², the survey contains ~ 450 galaxy clusters out to a redshift ~2 and to an X-ray flux limit of ~ 5 × 10⁻¹⁵ erg s⁻¹ cm⁻². This paper is part of the first release of XXL results focussed on the bright cluster sample.

Aims. We investigate the scaling relation between weak-lensing mass and X-ray temperature for the brightest clusters in XXL. The scaling relation discussed in this article is used to estimate the mass of all 100 clusters in XXL-100-GC.

Methods. Based on a subsample of 38 objects that lie within the intersection of the northern XXL field and the publicly available CFHTLenS shear catalog, we derive the weak-lensing mass of each system with careful considerations of the systematics. The clusters lie at 0.1 < z < 0.6 and span a temperature range of T ≈ 1 – 5 keV. We combine our sample with an additional 58 clusters from the literature, increasing the range to T ≈ 1 – 10 keV. To date, this is the largest sample of clusters with weak-lensing mass measurements that has been used to study the mass-temperature relation.

Results. The mass-temperature relation fit (M ∝ T^b) to the XXL clusters returns a slope b = 1.78^{+0.37}_{-0.32} and intrinsic scatter σ_{ln M/T} ≈ 0.53; the scatter is dominated by disturbed clusters. The fit to the combined sample of 96 clusters is in tension with self-similarity, b = 1.67 ± 0.12 and σ_{ln M/T} ≈ 0.41.

Conclusions. Overall our results demonstrate the feasibility of ground-based weak-lensing scaling relation studies down to cool systems of ~ 1keV temperature and highlight that the current data and samples are a limit to our statistical precision. As such we are unable to determine whether the validity of hydrostatic equilibrium is a function of halo mass. An enlarged sample of cool systems, deeper weak-lensing data, and robust modelling of the selection function will help to explore these issues further.

Key words. Keywords should be given

1. Introduction

Analytical and numerical calculations both predict that the temperature of the X-ray emitting atmospheres of galaxy groups and of clusters scales with the mass of their host dark matter halos,

with $M \propto T^{3/2}$ (Kaiser 1986; Evrard et al. 2002; Borgani et al. 2004). Testing this so-called self-similar prediction is of fundamental importance to a broad range of astrophysical and cosmological problems, including constraining any non-gravitational physics that affects the gas, and exploring galaxy clusters as probes of cosmological parameters.

To date, any studies of the mass-temperature relation have employed X-ray observations to measure both the temperature and the mass of galaxy groups and clusters. Assuming hydrostatic equilibrium, the self-similar predicted slope value of 1.5

[★] Based on observations obtained with XMM-Newton, an ESA science mission with instruments and contributions directly funded by ESA Member States and NASA. Based on observations made with ESO Telescopes at the La Silla Paranal Observatory under programme 089.A-0666 and LP191.A-0268

can be derived from the virial theorem. Observational relations, however, generally steepen from close to the self-similar for hot systems to a slope of $\sim 1.6 - 1.7$ when cooler systems ($T \lesssim 3$ keV) are included (see Böhringer et al. 2012; Giodini et al. 2013, for recent reviews). These results are subject to several problems, most prominently that the mass measurements are based on the assumption that the intracluster gas is in hydrostatic equilibrium and also that the same data are used for both temperature and mass measurements, likely introducing a subtle covariance into the analysis.

Independent measurements of mass and temperature, and reliance on fewer assumptions, help to alleviate these questions. Gravitational lensing mass measurements are useful in this regard, and have been shown to recover the ensemble mass of clusters to reasonably good accuracy (Becker & Kravtsov 2011; Bahé et al. 2012), despite concerns that individual cluster mass measurements may be affected by halo triaxiality and projection effects (e.g. Corless & King 2007; Meneghetti et al. 2010). Lensing based studies of the mass-temperature relation have so far obtained slopes that are consistent with the self-similar prediction, albeit with large statistical uncertainties (Smith et al. 2005; Bardeau et al. 2007; Hoekstra 2007; Okabe et al. 2010; Jee et al. 2011; Mahdavi et al. 2013). One of the limitations of these studies has been that they concentrate on relatively hot clusters, $T \gtrsim 4$ keV.

Building on the Leauthaud et al. (2010) weak-lensing study of the mass-luminosity relation of groups in the COSMOS survey, Kettula et al. (2013) recently pushed lensing-based studies of the mass-temperature relation into the group regime, $T \simeq 1 - 3$ keV. Combining ten groups with complementary measurements of massive clusters from the literature, they obtained a relation spanning $T \simeq 1 - 10$ keV, with a slope in good agreement with the self-similar prediction. This suggests that the assumption of hydrostatic equilibrium may be less valid in cooler systems than hotter systems since the discrepancy is only seen at the cool end of the $M_{\text{HSE}}-T$ relation. However, Connor et al. (2014) obtained a slope steeper than the hydrostatic results using a sample of 15 poor clusters. Their study was limited to cluster cores within r_{2500} (i.e. the radius at which the mean density of the cluster is 2500 times the critical density of the universe at the cluster redshift), in contrast to previous results (e.g. Kettula et al. 2013) that were derived within r_{500} , indicating that the mass-temperature relation may depend on the cluster centric radius within which the mass is measured.

We present the mass calibration of the XXL bright cluster sample (XXL-100-GC) based on a new mass-temperature relation that we constrain using the largest sample used to date for such studies: 96 groups and clusters spanning X-ray temperatures of $T \simeq 1 - 10$ keV and a redshift range of $z \simeq 0.1 - 0.6$. Thirty-eight of these systems come from XXL-100-GC itself. We combine the *XMM-Newton* survey data and the high-fidelity weak-shear catalog from the CFHTLenS survey to obtain independent temperature and halo mass measurements, respectively. We describe the sample, data, and analysis, including details on the weak gravitational lensing analyses, in Section 2. In Section 3 we present our main results, the mass-temperature relation of XXL-100-GC. We discuss a range of systematic uncertainties in our analysis, confirming that they are sub-dominant to the statistical uncertainties, in Section 4. We also compare our results with the literature in Section 4, and summarise our results in Section 5. We assume a WMAP9 (Hinshaw et al. 2013) cosmology of $H_0 = 70 \text{ km s}^{-1} \text{ Mpc}^{-1}$, $\Omega_M = 0.28$, and $\Omega_\Lambda = 0.72$. All statistical errors are reported to 68% significance and upper limits are stated at 3σ confidence.

2. Sample, data and analysis

2.1. Survey and sample definition

The XXL Survey is described in detail by Pierre et al. (2016, Paper I, hereafter). This $\sim 50 \text{ deg}^2$ *XMM-Newton* survey has a sensitivity of $\sim 5 \times 10^{-15} \text{ erg s}^{-1} \text{ cm}^{-2}$ in the [0.5-2] keV band that provides a well-defined galaxy cluster sample for precision cosmology. The survey is an extension of the 11 deg^2 XMM-LSS survey (Pierre et al. 2004) and consists of two 25 deg^2 areas. The XXL-100-GC¹ sample is a flux-limited sample based on 100 clusters ranked brightest in flux. It is described in detail by Pacaud et al. (2016, Paper II, hereafter), some of these clusters have previously been described in the XMM-LSS and XMM-BCS studies (Clerc et al. 2014; Šuhada et al. 2012). We note that five systems (XLSSC 113, 114, 115, 550, and 551) were observed in bad pointings that are contaminated by flaring. Subsequently, the sample was supplemented with five additional clusters: XLSSC 091, 506, 516, 545 and 548. All systems within the XXL-100-GC sample are characterised as either C1 or C2 (Clerc et al. 2014). The C1 objects have a high likelihood of detection and extension. The probability of contamination by spurious detection or point sources for these systems is low ($< 3\%$), whereas the C2 objects have $\sim 50\%$ contamination. The XXL-100-GC sample is estimated to be more than 99% complete down to $\sim 3 \times 10^{-14} \text{ erg s}^{-1} \text{ cm}^{-2}$ and to have spectroscopic redshifts of $0.05 \leq z \leq 1.07$ (Paper II).

The mass-temperature relation presented in this paper is based on weak-lensing mass measurements using the Canada-France-Hawaii Telescope Lensing Survey (CFHTLenS) shear catalogue² (Heymans et al. 2012; Erben et al. 2013). CFHTLenS spans a total survey area of $\sim 154 \text{ deg}^2$ that has considerable overlap with the northern XXL field (Fig. 1). Their shear catalogue comprises galaxy shape measurements for a source density of 17 galaxies per arcmin², as well as $u^*g'r'iz'$ -band photometry and photometric redshifts for the same galaxies. The median photometric redshift of the galaxies in the catalogue is $z_{\text{median}} = 0.75$ (Hilbrandt et al. 2012).

Fifty-two of the 100 XXL-100-GC sources lie in the northern XXL field, of which 45 lie within the CFHTLenS survey area (Fig. 1). A few of these 45 clusters lie at redshifts beyond the median redshift of the CFHTLenS shear catalogue, thus significantly reducing the number density of galaxies behind these distant clusters. We therefore limit our analysis to clusters at $z < 0.6$, which corresponds to imposing a lower limit on the source density of $\sim 4 \text{ arcmin}^{-2}$ (Fig. 3). This gives a total sample of 38 galaxy clusters for which we have a redshift, faint galaxy shape measurements, and an X-ray temperature (Table 1). All 38 of these galaxy clusters are classified as C1 with the exception of XLSSC114, which is a C2 class system.

2.2. X-ray temperatures

The temperature of the intracluster medium of each cluster is measured and described in detail by Giles et al. (2016, Paper III, hereafter). Here we summarise the key points pertaining to our analysis.

The spectra are extracted using a circular aperture of radius 0.3 Mpc centred on the X-ray positions, with a minimum of 5

¹ XXL-100-GC data are available in computer readable form via the XXL Master Catalogue browser <http://cosmosdb.iasf-milano.inaf.it/XXL> and via the XMM XXL Database <http://xmm-lss.in2p3.fr>

² www.cfhtlens.org

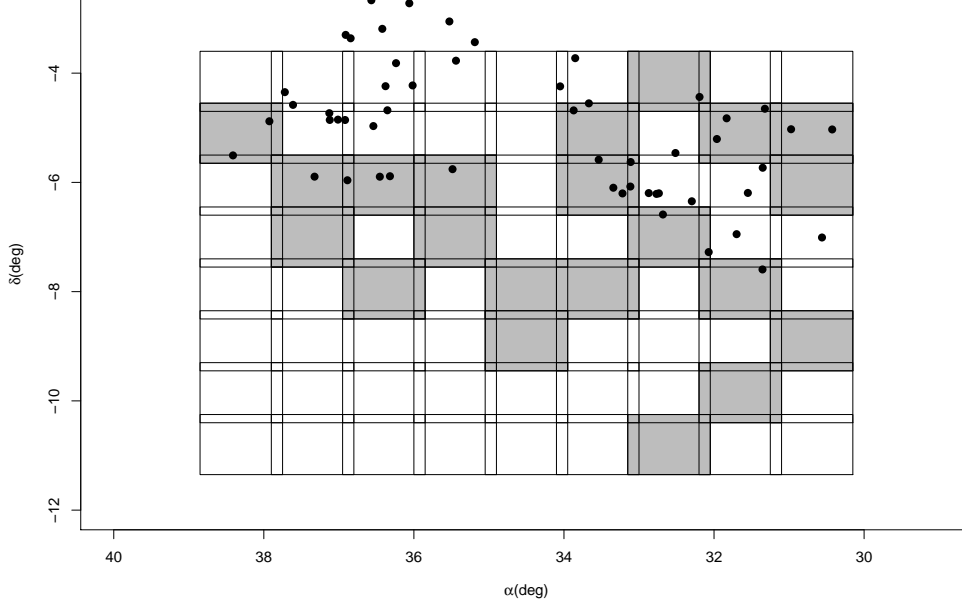


Fig. 1. Overlap of XXL-100-GC with the CFHTLenS W1 field. The boxes are individual pointings in CFHT with XXL-North field clusters (filled points). The shaded boxes are pointings that fail the CFHTLenS weak-lensing field selection criteria (See section 4.1).

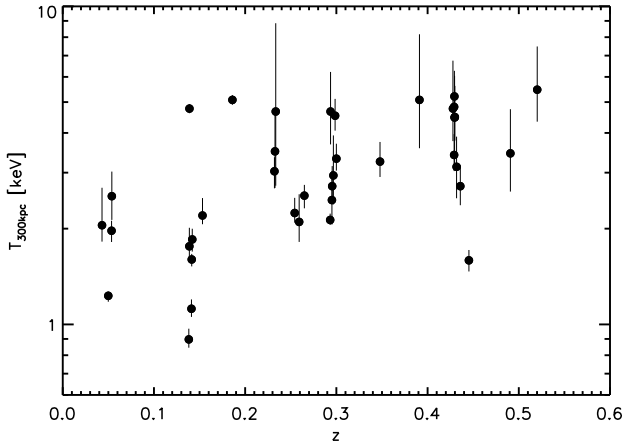


Fig. 2. Redshift versus X-ray temperature $T_{300\text{kpc}}$ for the 38 clusters from XXL-100-GC that are located within the CFHTLenS shear catalogue footprint.

counts bin^{-1} . Point sources are identified using SExtractor and excluded from the analysis; the images are visually inspected for any that might have been missed. Radial profiles of each source were extracted within the $0.5 - 2$ keV band with the background subtracted. The detection radius was defined as the radius at which the source is detected to 0.5σ above the background. Background regions were taken as annuli centred on the observation centre with a width equal to the spectral extraction region and the region within the detection radius excluded. Where this was not possible, the background was measured from an annulus centred on the cluster with inner radius set to the detection radius and outer radius as 400 arcsec.

The X-ray temperatures span $1.1 \text{ keV} \leq T_{300\text{kpc}} < 5.5 \text{ keV}$ (Figure 2) and are non-core excised owing to the limited angular resolution of *XMM-Newton*. The temperatures are extracted within a fixed physical radius of 0.3 Mpc such that they are straightforward to calculate from shallow survey data without needing to estimate the size of the cluster. This is the largest radius within which it is possible to measure a temperature for the whole XXL-100-GC sample. To check the sensitivity of our main results to this choice of aperture, we also re-fit the mass-temperature relation discussed in the results section using the temperatures that are available in larger apertures up to 0.5 Mpc, and find that the systematic differences between the respective fit parameters are negligible compared with the statistical errors on the fits.

2.3. Cool core strength

The cool core strength of XXL-100-GC is estimated by Démoclès, et al. (in prep.) using the concentration parameter method of Santos et al. (2008). We summarise a few key points of the analysis here. The X-ray surface brightness profile is extracted within concentric annuli centred on the X-ray peak, it is both background-subtracted and exposure corrected and then re-binned to obtain a minimum signal-to-noise ratio (S/N) of 3 in each bin. The profiles are fit using three 3D density profile models which are projected on the sky and convolved with the *XMM-Newton* point spread function (PSF). Depending on the number of bins in the surface brightness profile (n_{bin}), a more or less flexible β -model is fit to the data: $\beta = 2/3$ is assumed for profiles with $n_{\text{bin}} < 3$; β is a free parameter for $3 \leq n_{\text{bin}} \leq 4$; a double β model is used for $n_{\text{bin}} > 4$. The surface brightness concentration parameter (CSB) is defined as the ratio of the integrated profile within 40 kpc to that within 400

kpc, $\text{CSB} = \text{SB}(<40 \text{ kpc}) / \text{SB}(<400 \text{ kpc})$. The cool core status is defined as

- Non-cool core: $\text{CSB} < 0.075$
- Weak cool core: $0.075 \leq \text{CSB} \leq 0.155$
- Strong cool core: $\text{CSB} > 0.155$

2.4. Weak gravitational lensing

We use the full photometric redshift probability distribution, $P(z)$, of each galaxy in the CFHTLenS shear catalogue to identify galaxies behind our cluster sample. Galaxies are selected as background galaxies if they satisfy

$$z_s - \delta z_s(3\sigma) > z + 0.01, \quad (1)$$

where z_s is the peak of the respective galaxy's $P(z)$, z is the cluster redshift, $\delta z_s(3\sigma)$ is the 99.7% lower confidence interval on z_s , and the last term represents a velocity offset of 3000 km s^{-1} as a conservative allowance for the velocity width of the cluster galaxy distributions.

The method outlined in Velandar et al. (2014) and Miller et al. (2013) is used to calibrate the gravitational shear measurements. The raw ellipticity values (e_1, e_2) undergo two calibration corrections, a multiplicative component (m) derived from simulations (Miller et al. 2013) and an additive component (c) derived from the data (Heymans et al. 2012). The observed ellipticity can be written as

$$e^{\text{obs}} = (1 + m)e^{\text{int}} + c + \Delta e \quad (2)$$

where e^{int} is the intrinsic ellipticity and Δe is the noise on the measurement.

The multiplicative component m is dependent on both galaxy size and S/N and gives, on average, a 6% correction. The additive component c is similarly dependent on the galaxy size, and the S/N determined by Lensfit. For the CFHTLenS data $\langle c_1 \rangle$ is consistent with zero and c_2 is subtracted from e_2 for each galaxy. The multiplicative correction is applied as an average ensemble of each bin.

A weighting is also applied that corrects for the geometry of the lens-source system in the form of the lensing kernel $\xi = D_{\text{LS}}/D_s$, where D_{LS} and D_s are the angular diameter distances between the lens and the source, and between the observer and the source, respectively. This is applied as a ratio between that of the cluster-galaxy system and that of the reference $\eta = \xi/\xi_{\text{ref}}$. The reference is taken as the mode source redshift of the sum of all background galaxy weighted $P(z_s)$, i.e. the mode of

$$n(z_s) = \sum_{i=1}^{N_{\text{gal}}} w_i P_i(z_s) \quad (3)$$

where w_i is the CFHTLenS inverse variance weight (Miller et al. 2013, equation 8) applied to calibrate for the likelihood of the measured ellipticity and intrinsic shape noise. The calibrated shear at a distance r from the cluster centre therefore takes the form

$$\langle \gamma(r)^{\text{cal}} \rangle = \frac{\sum_{i=1}^{N_{\text{gal}}} w_i \eta_i \gamma_i^{\text{int}} \sum_{i=1}^{N_{\text{gal}}} w_i \eta_i}{\sum_{i=1}^{N_{\text{gal}}} w_i \eta_i (1 + m_i) \sum_{i=1}^{N_{\text{gal}}} w_i \eta_i^2} \quad (4)$$

In the weak-lensing limit the shear can be estimated as the average complex ellipticity $\gamma \approx \langle e \rangle$, where $e \equiv e_1 + i e_2$. In terms of tangential and cross-component ellipticity,

$$e_+ = -\Re e^{-2i\phi} = -(e_2 - c_2) \sin(2\phi) - e_1 \cos(2\phi) \quad (5)$$

$$e_\times = -\Im e^{-2i\phi} = e_1 \sin(2\phi) - (e_2 - c_2) \cos(2\phi) \quad (6)$$

where the tangential shear, $e_+(r)$, is the signal that can be modelled in terms of the total matter density profile of the lens. The cross shear $e_\times(r)$ is orientated 45° with respect to the tangential component and should be consistent with zero as a check on systematic errors.

We extract the shear profile of each cluster within a 0.15 – 3 Mpc annulus. The inner radial cut helps to ameliorate centring uncertainties, and the outer radial cut is motivated by numerical simulations (Becker & Kravtsov 2011). The cluster centre is taken as the X-ray centroid. For reference, the mean offset between the X-ray centroid and the brightest cluster galaxy (BCG) is $\langle \delta r \rangle = 64.7 \text{ kpc}$. Our results are unchanged if we centre the shear profiles on the respective BCGs (see section 4.1 for more details).

The shear is binned in eight radial bins equally spaced in log and with a lower limit of 50 galaxies per radial bin. If this threshold is not met, the bin is combined with the next radial bin. The errors on the shear in each radial bin are estimated from 10^3 bootstrap resamples with replacement and includes the large scale structure covariance (Schneider et al. 1998):

$$C_{ij}^{LSS} = \int P_k(l) J_2(l\theta_i) J_2(l\theta_j) \frac{ldl}{2\pi}, \quad (7)$$

where $P_k(l)$ is the weak-lensing power spectrum as a function of angular multipole l and $J_2(l\theta)$ is the second-order Bessel function of the first type at radial bins θ_i and θ_j .

Shear S/N is calculated following Okabe et al. (2010) as

$$(S/N)^2 = \sum_{n=1}^{N_{\text{bin}}} \frac{\langle e_+(r_n) \rangle^2}{\sigma_{e_+}^2(r_n)}. \quad (8)$$

For our sample the weak-lensing S/N ranges from $1 \leq S/N \leq 7$. However we include all objects in the mass-temperature relation regardless of the S/N value to avoid imposing a low-shear selection on top of the original X-ray selection.

We model the shear profile as a (Navarro et al. 1997, NFW hereafter) profile following the formalism set out by Wright & Brainerd (2000). A Markov chain Monte Carlo (MCMC) sampler with a Gaussian likelihood is used to fit the NFW model to the shear profile. The algorithm returns 5×10^4 samples of the target distribution using a jump proposal based on a Metropolis-Hastings algorithm with a mean acceptance rate of 0.57. The autocorrelation length is computed to thin correlated samples within the chain and incorporates burn-in of 150 samples. The Gelman-Rubin criterion (Gelman and Rubin 1992) is computed for three chains to ensure convergence. The mass of each cluster is taken as the mode of the posterior and the errors are given as 68% credible regions of the highest posterior density as this is the best representation of the skewed Gaussian posteriors.

Given the wide range of possible cluster mass, a uniform in log (Jeffreys) prior is used to ensure scale invariance $P(M|I) = \frac{1}{M \ln(10^{16}/10^{13})}$ ($10^{13} \leq M_{200} \leq 10^{16} M_\odot$). Given the generally low-shear S/N, we fix cluster concentration to values from a mass-concentration relation based on N-body simulations (Duffy et al. 2008):

$$c_{200} = 5.71(1 + z)^{-0.47} \left(\frac{M_{200}}{2 \times 10^{12} h^{-1} M_\odot} \right)^{-0.084} \quad (9)$$

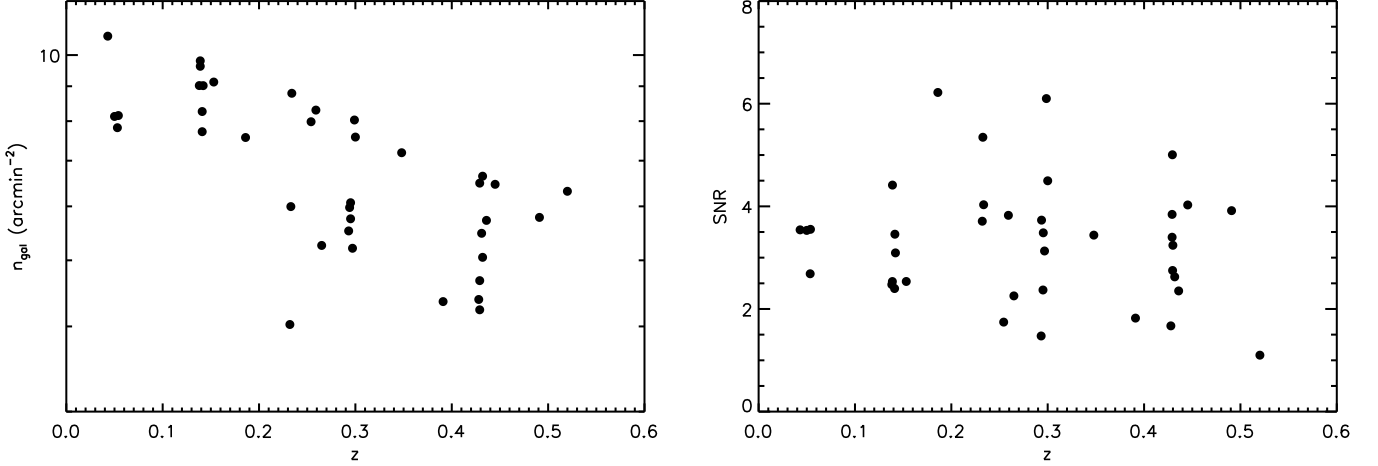


Fig. 3. LEFT: Number density of background galaxies behind each galaxy cluster versus cluster redshift. RIGHT: Weak-lensing shear signal-to-noise ratio as a function of cluster redshift.

We test the sensitivity of our results to the choice of this relation and find that it is not a dominant source of uncertainty (see section 4.1 for more details).

To estimate $M_{\Delta, \text{WL}}$ for each cluster we integrate the NFW model out to the radius at which the mean density of the halo is $\Delta\rho_{\text{crit}}(z)$, where z is the cluster redshift (Table 1) and $\Delta=500$:

$$\begin{aligned} M_{\Delta, \text{WL}} &= \int_0^{r_{\Delta, \text{WL}}} \rho(r) 4\pi r^2 dr \\ &= 4\pi\rho_s r_s^3 \left[\ln\left(1 + \frac{r_{\Delta, \text{WL}}}{r_s}\right) - \frac{r_{\Delta, \text{WL}}}{r_s + r_{\Delta, \text{WL}}} \right]. \end{aligned} \quad (10)$$

3. Results

A positive correlation between our weak-lensing mass and X-ray temperature measurements is evident (Figure 4). In this section, we define the scaling relation model that we will fit to the data, describe the regression analysis, and present the main results. We defer consideration of possible systematic uncertainties and comparison with the literature to section 4.

3.1. XXL mass-temperature relation

We model the mass–temperature relation as a power law:

$$\log_{10} \left(\frac{M_{500} E(z)}{M_{\odot} h_{70}^{-1}} \right) = a + b \log_{10} \left(\frac{T}{\text{keV}} \right) \quad (11)$$

with intercept a and slope b , where $E(z) = \sqrt{\Omega_m(1+z)^3 + \Omega_{\Lambda}}$ describes the evolution of the Hubble parameter. We note that by not allowing any freedom in the exponent of $E(z)$, we are assuming self-similar evolution. This is motivated by the large scatter which is apparent in our data, that precludes us from constraining evolution at this time.

For the linear regression we use the Gibbs sampler implemented in the multivariate Gaussian mixture model routine `linmix_err` (Kelly 2007) with the default of three Gaussians. We use 10^5 random draws of the sampler and take the fitted parameters as the posterior mode and the error as the 68% highest posterior density credible interval. When the number of data

points is small, the Gibbs sampler will have difficulty in reaching convergence. `linmix_err` also has the option of running as a Metropolis-Hastings algorithm, which is more efficient for small sample size. Tests implementing the Metropolis-Hastings algorithm give consistent results.

We fit the model to the measured values of $M_{500, \text{WL}}$ and $T_{300\text{kpc}}$. For some galaxy clusters, the weak-lensing S/N is so low that we are only able to obtain an upper limit on $M_{500, \text{WL}}$. The posteriors of these systems are truncated by the lower bound prior on mass. Despite this, it is important to include these systems in the fit because they are X-ray detected at high significance, and to exclude them would add a further selection in addition to the primary X-ray selection. The fitting method used is able to incorporate upper limits as censored data using a likelihood that integrates over the censored and uncensored data separately (see Kelly 2007, for more details). However their implementation is not suitable for our problem since we have prior knowledge of the X-ray detection we know that these systems should have a mass greater than $10^{13} M_{\odot}$, flagging them as censored data would contradict the mass prior used in fitting the NFW profile. Tests to recover scaling relation parameters on simulated toy data show that censoring leads to a positive bias in the slope. For systems where the lower credible region is truncated by the mass prior and hence underestimated we set the lower mass error equal to the upper mass error. In our toy model tests this gave the least bias in scaling relation parameters, with biases $< 10\%$.

The mass-temperature relation based on the 38 clusters that overlap between the XXL-100-GC and the CFHTLenS shear catalog has a slope of $b = 1.78^{+0.37}_{-0.32}$, with an intrinsic scatter in natural log of mass at fixed temperature of $\sigma_{\text{int ln M|T}} \simeq 0.5$ (Table 2).

3.2. Cool core status and dynamical disturbance

We investigate whether the mass-temperature relation fit parameters depend on the strength of cooling in the clusters cores and the dynamical state of the clusters.

First, we collectively classify weak and strong cool cores as cool core systems and fit the mass-temperature relation to this cool core subsample, and the non-cool core subsample. The results of the fits have large statistical uncertainties and intrinsic

Table 1. Cluster properties and mass estimates.

Name	z	$T_{300\text{kpc}}$ (keV)	c_{200}	$M_{200,\text{WL}}$ ($10^{14}h_{70}^{-1}M_{\odot}$)	$M_{500,\text{WL}}$ ($10^{14}h_{70}^{-1}M_{\odot}$)	$r_{500,\text{WL}}$ (Mpc)	δr (10^{-2}Mpc)	$\delta r/r_{500,\text{WL}}$ (10^{-1})	CSB (10^{-2})	SNR
(1)	(2)	(3)	(4)	(5)	(6)	(7)	(8)	(9)	(10)	(11)
XLSSC 006	0.429	4.8 ^{+0.5} _{-0.4}	2.7	5.3 ^{+6.0} _{-2.3}	3.4 ^{+3.7} _{-1.4}	0.9 ^{+0.3} _{-0.2}	10.1	1.1	8.0 ± 1.0	3.4
XLSSC 011	0.054	2.5 ^{+0.5} _{-0.4}	3.4	1.6 ^{+2.0} _{-1.1}	1.1 ^{+1.3} _{-0.7}	0.7 ^{+0.2} _{-0.2}	0.4	0.1	12.7 ± 0.9	3.6
XLSSC 022	0.293	2.1 ^{+0.1} _{-0.1}	3.4	0.5 ^{+0.9} _{-0.4}	0.4 ^{+0.5} _{-0.2}	0.5 ^{+0.2} _{-0.1}	4.5	1.0	34.6 ± 2.6	1.5
XLSSC 025	0.265	2.5 ^{+0.2} _{-0.2}	3.1	1.7 ^{+1.6} _{-1.3}	1.1 ^{+1.0} _{-0.8}	0.7 ^{+0.2} _{-0.2}	0.0	0.0	27.9 ± 2.7	2.3
XLSSC 027	0.295	2.7 ^{+0.4} _{-0.3}	2.9	3.3 ^{+3.9} _{-0.9}	2.1 ^{+2.4} _{-1.4}	0.8 ^{+0.2} _{-0.2}	8.1	1.0	4.7 ± 2.5	3.5
XLSSC 041	0.142	1.9 ^{+0.3} _{-0.2}	3.4	1.0 ^{+0.9} _{-0.7}	0.7 ^{+0.5} _{-0.5}	0.6 ^{+0.2} _{-0.2}	1.3	0.2	29.9 ± 2.5	3.1
XLSSC 054	0.054	2.0 ^{+0.2} _{-0.2}	3.5	1.1 ^{+1.6} _{-0.7}	0.7 ^{+1.1} _{-0.5}	0.6 ^{+0.2} _{-0.2}	0.5	0.1	11.1 ± 1.3	2.7
XLSSC 055	0.232	3.0 ^{+0.3} _{-0.3}	2.8	8.1 ^{+7.6} _{-3.1}	5.2 ^{+4.7} _{-2.0}	1.1 ^{+0.3} _{-0.2}	4.2	0.4	11.3 ± 1.9	3.7
XLSSC 056	0.348	3.2 ^{+0.5} _{-0.3}	2.8	4.5 ^{+2.7} _{-2.4}	2.8 ^{+1.7} _{-1.5}	0.9 ^{+0.2} _{-0.2}	6.4	0.7	5.6 ± 1.7	3.4
XLSSC 057	0.153	2.2 ^{+0.3} _{-0.1}	3.7	≤ 0.9	≤ 0.6	≤ 0.6	3.0	0.7	17.1 ± 1.8	2.5
XLSSC 060	0.139	4.8 ^{+0.2} _{-0.2}	3.2	2.1 ^{+1.4} _{-1.5}	1.4 ^{+0.9} _{-1.0}	0.8 ^{+0.1} _{-0.3}	13.5	1.8	2.3 ± 0.1	4.4
XLSSC 061	0.259	2.1 ^{+0.5} _{-0.3}	2.9	3.8 ^{+0.9} _{-3.1}	2.4 ^{+0.5} _{-1.3}	0.9 ^{+0.1} _{-0.2}	2.9	0.3	9.9 ± 3.3	3.8
XLSSC 083	0.430	4.5 ^{+1.1} _{-0.7}	2.7	4.0 ^{+3.6} _{-2.8}	2.5 ^{+2.2} _{-0.7}	0.8 ^{+0.2} _{-0.2}	4.1	0.5	7.0 ± 2.4	3.2
XLSSC 084	0.430	4.5 ^{+1.6} _{-1.3}	2.7	4.3 ^{+3.2} _{-3.2}	2.7 ^{+1.9} _{-2.0}	0.9 ^{+0.2} _{-0.3}	10.9	1.3	3.0 ± 0.7	2.8
XLSSC 085	0.428	4.8 ^{+2.0} _{-1.0}	3.2	≤ 2.6	≤ 1.21	≤ 0.7	0.0	0.0	10.6 ± 4.3	1.7
XLSSC 087	0.141	1.6 ^{+0.1} _{-0.1}	3.6	0.5 ^{+0.4} _{-0.4}	0.3 ^{+0.3} _{-0.2}	0.5 ^{+0.1} _{-0.1}	0.9	0.2	41.5 ± 2.9	3.5
XLSSC 088	0.295	2.5 ^{+0.6} _{-0.4}	3.1	1.8 ^{+1.3} _{-1.5}	1.2 ^{+0.9} _{-0.9}	0.7 ^{+0.1} _{-0.3}	28.2	4.2	2.7 ± 0.4	2.4
XLSSC 090	0.141	1.1 ^{+0.1} _{-0.1}	4.1	≤ 0.6	≤ 1.2	≤ 0.7	0.9	0.3	41.7 ± 4.2	2.4
XLSSC 091	0.186	5.1 ^{+0.2} _{-0.8}	2.8	9.7 ^{+3.3} _{-2.9}	6.2 ^{+2.1} _{-1.8}	1.2 ^{+0.1} _{-0.1}	5.0	0.4	2.5 ± 0.1	6.2
XLSSC 092	0.432	3.1 ^{+0.8} _{-0.6}	3.2	≤ 2.2	≤ 1.4	≤ 0.7	26.3	7.9	6.9 ± 1.7	2.6
XLSSC 093	0.429	3.4 ^{+0.6} _{-0.4}	2.7	5.9 ^{+3.5} _{-3.0}	3.7 ^{+2.1} _{-1.8}	0.9 ^{+0.2} _{-0.2}	2.9	0.3	5.4 ± 1.6	3.8
XLSSC 095	0.138	0.9 ^{+0.1} _{-0.1}	3.6	≤ 1.0	≤ 0.6	≤ 0.6	0.0	0.0	40.3 ± 14.9	2.5
XLSSC 096	0.520	5.5 ^{+2.0} _{-1.1}	3.5	≤ 1.4	≤ 0.9	≤ 0.6	5.0	1.7	7.3 ± 2.5	1.1
XLSSC 098	0.297	2.9 ^{+1.0} _{-0.6}	3.0	2.8 ^{+3.6} _{-2.3}	1.8 ^{+2.3} _{-1.5}	0.8 ^{+0.2} _{-0.3}	2.3	0.3	17.1 ± 6.7	3.1
XLSSC 099	0.391	5.1 ^{+3.1} _{-1.5}	3.5	≤ 2.2	≤ 1.4	≤ 0.7	1.9	0.6	6.6 ± 1.8	1.8
XLSSC 103	0.233	3.5 ^{+1.2} _{-0.8}	2.8	8.5 ^{+4.2} _{-3.0}	5.4 ^{+2.6} _{-1.8}	1.1 ^{+0.2} _{-0.3}	4.2	0.4	6.9 ± 2.6	5.3
XLSSC 104	0.294	4.7 ^{+1.5} _{-1.0}	3.0	2.6 ^{+3.0} _{-1.3}	1.7 ^{+1.8} _{-0.9}	0.8 ^{+0.3} _{-0.2}	14.9	2.0	9.9 ± 3.7	3.7
XLSSC 105	0.429	5.2 ^{+1.1} _{-0.8}	2.4	19.8 ^{+6.5} _{-7.7}	12.1 ^{+3.9} _{-4.6}	1.4 ^{+0.1} _{-0.2}	14.3	1.0	3.5 ± 0.7	5.0
XLSSC 106	0.300	3.3 ^{+0.4} _{-0.3}	2.8	6.8 ^{+3.0} _{-3.3}	4.3 ^{+1.8} _{-2.1}	1.0 ^{+0.1} _{-0.3}	27.2	2.6	7.0 ± 1.3	4.5
XLSSC 107	0.436	2.7 ^{+0.4} _{-0.3}	2.8	2.8 ^{+4.8} _{-2.2}	1.8 ^{+3.0} _{-1.4}	0.7 ^{+0.3} _{-0.3}	0.0	0.0	13.0 ± 2.6	2.4
XLSSC 108	0.254	2.2 ^{+0.3} _{-0.2}	3.9	≤ 0.9	≤ 0.6	≤ 0.5	4.0	1.3	14.0 ± 2.5	1.7
XLSSC 109	0.491	3.5 ^{+1.3} _{-0.8}	2.6	7.6 ^{+6.6} _{-4.5}	4.7 ^{+4.0} _{-2.8}	1.0 ^{+0.2} _{-0.3}	3.1	0.3	60.5 ± 19.7	3.9
XLSSC 110	0.445	1.6 ^{+0.1} _{-0.1}	2.7	4.6 ^{+5.3} _{-1.6}	2.9 ^{+3.2} _{-1.8}	0.9 ^{+0.2} _{-0.2}	17.7	2.0	2.6 ± 0.4	4.0
XLSSC 111	0.299	4.5 ^{+0.6} _{-0.5}	2.7	10.1 ^{+3.6} _{-2.9}	6.3 ^{+1.8} _{-1.8}	1.2 ^{+0.1} _{-0.1}	1.6	0.1	13.8 ± 4.5	6.1
XLSSC 112	0.139	1.8 ^{+0.2} _{-0.2}	3.4	1.2 ^{+0.9} _{-0.8}	0.8 ^{+0.6} _{-0.5}	0.6 ^{+0.1} _{-0.2}	6.9	1.1	9.3 ± 1.5	2.5
XLSSC 113	0.050	1.2 ^{+0.0} _{-0.1}	3.9	0.4 ^{+0.6} _{-0.2}	0.3 ^{+0.4} _{-0.2}	0.5 ^{+0.2} _{-0.1}	0.4	0.1	19.4 ± 2.9	3.5
XLSSC 114	0.234	4.7 ^{+4.2} _{-1.9}	3.1	2.1 ^{+1.9} _{-1.0}	1.4 ^{+1.3} _{-0.6}	0.7 ^{+0.2} _{-0.1}	5.5	0.8	5.0 ± 1.9	4.0
XLSSC 115	0.043	2.1 ^{+0.6} _{-0.2}	4.3	≤ 0.6	≤ 0.4	≤ 0.5	2.5	0.8	6.9 ± 2.3	3.5

Column 1 is the cluster catalogue id number; Col. 2 is the cluster redshift; Col. 3 X-ray temperature measured within an aperture of 300 kpc; Col. 4 is the concentration parameter measured within $r_{200,\text{WL}}$; Cols. 5 and 6 are fitted estimates of weak-lensing mass centred on the X-ray centroid and measured within fitted $r_{200,\text{WL}}$ and $r_{500,\text{WL}}$ respectively. Upper limits on mass are given at 3 sigma confidence. Cols. 7 and 8 are the weak-lensing $r_{500,\text{WL}}$ and the offset between the X-ray centroid and the BCG; Col. 9 is the the BCG offset as a fraction of $r_{500,\text{WL}}$; Col. 10 is the CSB parameter and Col. 11 is the signal-to-noise ratio on the weak-lensing shear. Positions of the cluster X-ray centroids are listed in Paper II Table 1.

scatter. The same is true if we repeat the fits to the two subsamples holding the slope of the respective relations fixed at the self-similar value of $b = 1.5$ (Table 2).

Second, we use the offset between the X-ray centroid and the BCG (Lavoie et al. in prep.), expressed as a fraction of $r_{500,\text{WL}}$, to classify clusters as undisturbed $\delta r/r_{500,\text{WL}} < 0.05$, and disturbed $\delta r/r_{500,\text{WL}} > 0.05$. The scatter in the mass-temperature relation for undisturbed clusters is less than that of the disturbed clusters, albeit with large uncertainties. We see similar results if we hold the slope of the relation fixed at self-similar, as above. This suggests that the disturbed clusters dominate the scatter in the XXL-100 mass-temperature relation.

It is tempting to attribute the large scatter in the mass-temperature relation for disturbed clusters to the physics of the cluster merger activity implied by a large value of $\delta r/r_{500,\text{WL}}$. However we caution that dynamically active clusters likely have more complicated mass distributions than less active (“undisturbed”) clusters. Our ability to constrain reliable cluster mass measurements in the $10^{13} < M_{500} < 10^{14}M_{\odot}$ regime with low SNR survey data is likely a function of the complexity of the mass distribution. This mass range has not yet been explored to any great extent by simulation studies (e.g. Becker & Kravtsov 2011; Bahé et al. 2012). We will return to this question in a future article.

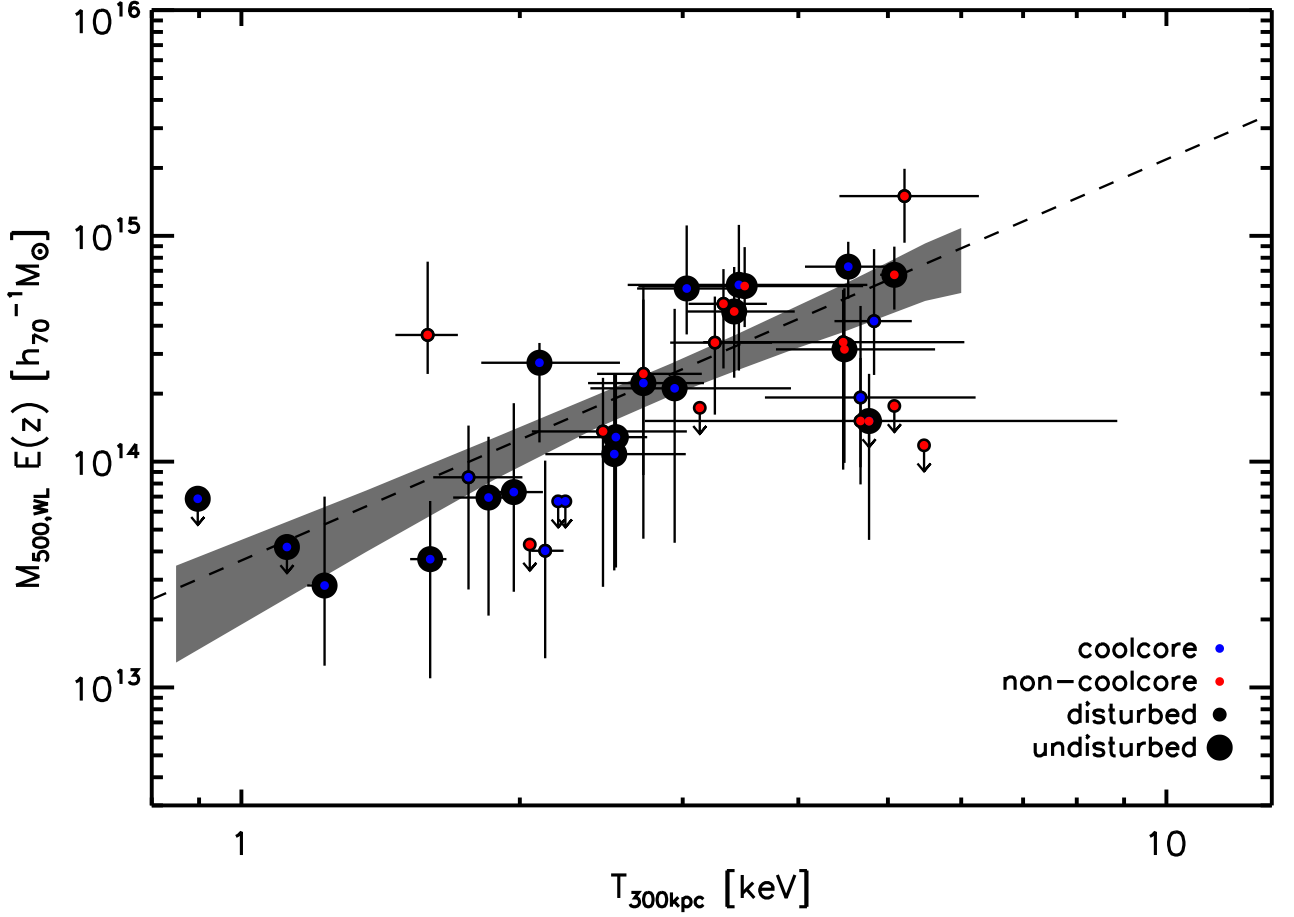


Fig. 4. The mass-temperature relation for 38 clusters drawn from XXL-100-GC for which weak-shear information is available from CFHTLenS. The line is the highest posterior density fit and the shaded region is the credible region. Systems with upper limits on mass are indicated by arrows and plotted at 3σ confidence.

3.3. Combination with other samples

To improve the precision and to extend the dynamic range of our mass-temperature relation we now include 10 groups from COSMOS (Kettula et al. 2013) and 48 massive clusters from the Canadian Cluster Comparison Project (CCCP; Mahdavi et al. (2013); Hoekstra et al. (2015)). The COSMOS groups are X-ray selected and their weak-lensing masses are based on deep *Hubble Space Telescope* observations, and follow a similar analysis method to our own. Unlike our sample, the temperatures of the COSMOS systems are core excised. We have therefore measured non-core excised temperatures for the ten COSMOS groups within the same 0.3Mpc measurement aperture using the same analysis process described in section 2.2. Comparison between these non-core excised temperature and the core excised temperatures used by Kettula et al. (2013) reveals a bias of $\langle T_{300\text{kpc}}/T_{0.1-0.5r_{500,\text{WL}}} \rangle = 0.91 \pm 0.05$ (Figure 7), and emphasise the importance of ensuring that the temperatures are measured in a consistent manner when combining samples.

We also obtained non-core excised temperatures for the CCCP clusters analysed by Mahdavi et al. (2013) from the CCCP web-site³, albeit within a 0.5 Mpc aperture. This is larger than the aperture that we use for our own temperature measure-

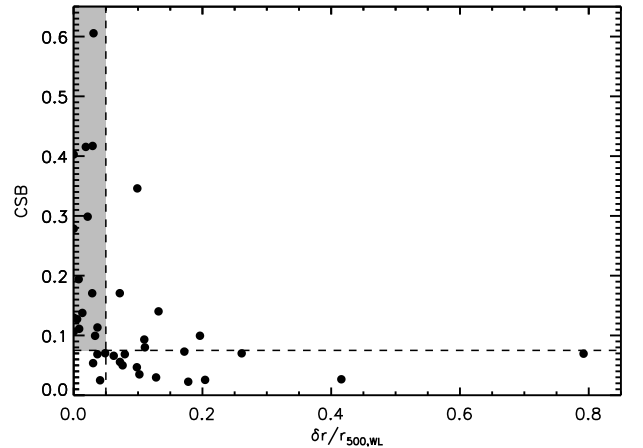


Fig. 6. CSB parameter versus the offset between X-ray centroid and BCG as a fraction of weak-lensing $r_{500,\text{WL}}$. The horizontal dashed line at $\text{CSB} = 0.075$ indicates the separation of cool core and non-cool core classed systems. The vertical dashed line at $\delta r / r_{500,\text{WL}} = 0.05$ separates undisturbed and disturbed clusters. The grey shaded region shows the overlap between cool core and undisturbed clusters.

³ <http://sfstar.sfsu.edu/cccp/>

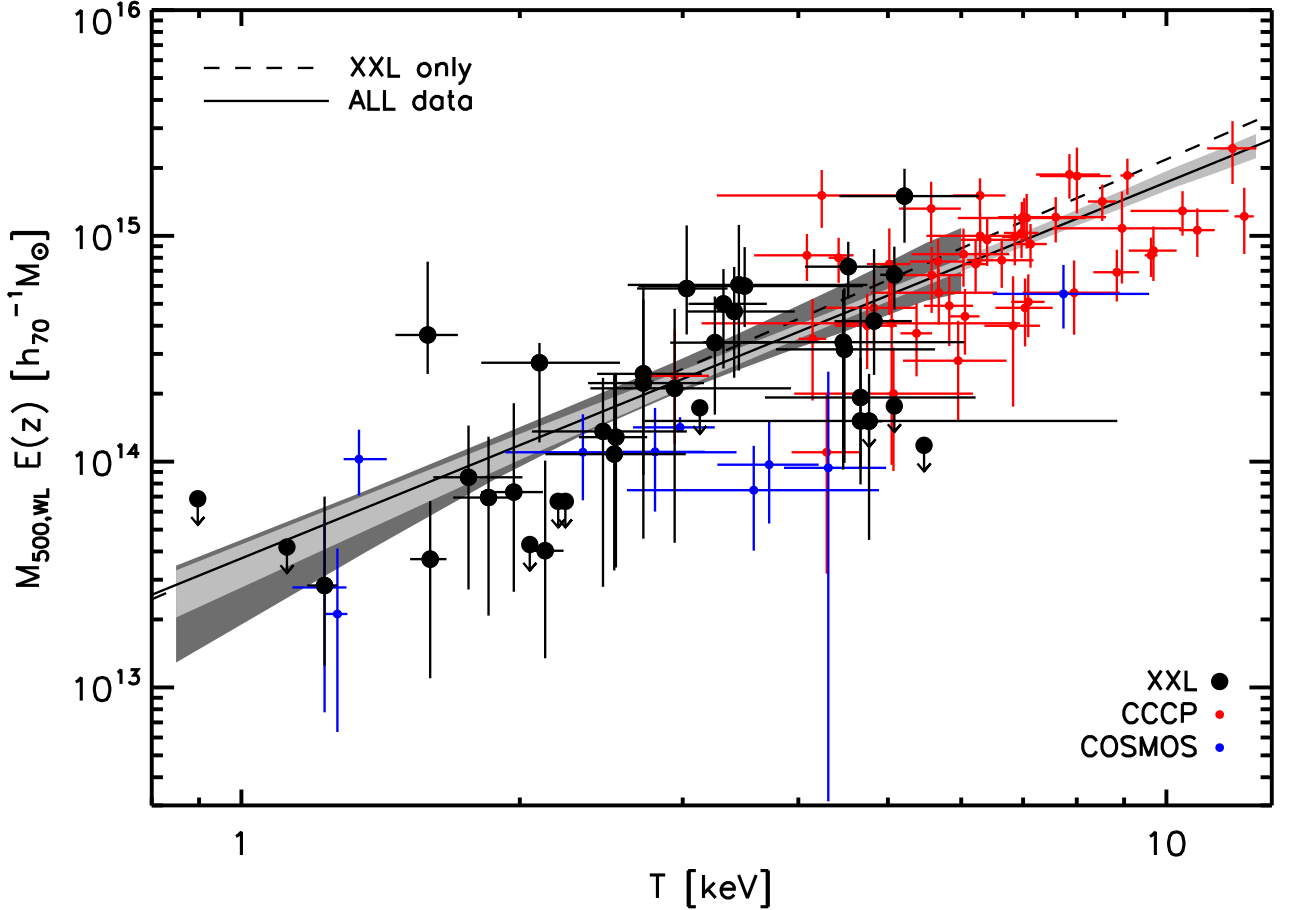


Fig. 5. Mass-temperature relation for the extended sample, including 38 systems from XXL (black), 10 from COSMOS (blue), and 48 from CCCP (red). The solid line and light gray shaded region are the best fit scaling relation and 68% credible interval for the XXL+CCCP+COSMOS sample. The dashed line and dark gray shaded region are the best fit and credible region for the XXL only sample. Systems with upper limits on mass are indicated by arrows and plotted at 3 sigma confidence.

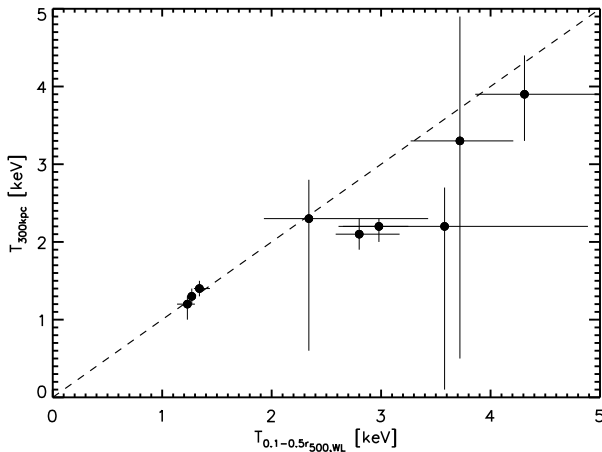


Fig. 7. Comparison of core excised X-ray temperatures (Kettula et al. 2013) and the re-derived temperatures measured within a 0.3Mpc aperture. The dashed line is equality.

ments. Given that the CCCP systems are more massive than ours,

we do not expect this difference in aperture to have a significant affect on our results. We confirm that this is indeed the case (see section 4.1 for more details).

We fit the mass-temperature relation to the joint data set following the same procedure as applied to the XXL-only sample in §3.1. The statistical precision of the fit is much higher than that of the XXL-only fit, and has very similar central values for all fit parameters between the two fits (Table 3). The slope parameter of the joint fit is $b = 1.67^{+0.14}_{-0.10}$ with an intrinsic scatter of $\sigma_{\text{int}(\ln M|T)} = 0.41^{+0.07}_{-0.06}$.

3.4. Mass estimates for XXL-100-GC

The mass of each member of XXL-100-GC is computed from the joint XXL+CCCP+COSMOS mass-temperature relation (see Table 2). The uncertainties on these masses are estimated by propagating uncertainties on individual temperature measurements, and the intrinsic scatter on the mass-temperature relation. The masses are presented in Paper II, and denoted as $M_{500,MT}$ to indicate that they are based on the mass-temperature scaling relation.

Table 2. Mass-temperature relation fit parameters for equation 11. Fixed slope relations are denoted by FS.

sample	intercept	slope	intrinsic scatter	N
	(a)	(b)	($\sigma_{\text{int ln } M/T}$)	
XXL	$13.56^{+0.16}_{-0.17}$	$1.78^{+0.37}_{-0.32}$	$0.53^{+0.21}_{-0.17}$	38
XXL+COSMOS+CCCP	$13.57^{+0.09}_{-0.09}$	$1.67^{+0.14}_{-0.10}$	$0.41^{+0.07}_{-0.06}$	96
XXL FS	$13.67^{+0.07}_{-0.03}$	1.50	$0.48^{+0.19}_{-0.08}$	38
XXL cool core	$13.46^{+0.19}_{-0.24}$	$1.81^{+0.43}_{-0.57}$	$0.64^{+0.26}_{-0.23}$	21
XXL non-cool core	$14.18^{+0.46}_{-0.39}$	$0.75^{+0.76}_{-0.73}$	$0.50^{+0.30}_{-0.22}$	17
XXL undisturbed	$13.56^{+0.15}_{-0.19}$	$1.86^{+0.35}_{-0.36}$	$0.34^{+0.25}_{-0.20}$	19
XXL disturbed	$13.67^{+0.40}_{-0.49}$	$1.49^{+0.82}_{-0.89}$	$0.91^{+0.28}_{-0.32}$	19
XXL cool core FS	$13.59^{+0.04}_{-0.08}$	1.50	$0.72^{+0.03}_{-0.16}$	21
XXL non-cool core FS	$13.83^{+0.04}_{-0.17}$	1.50	$0.50^{+0.15}_{-0.14}$	17
XXL undisturbed FS	$13.71^{+0.09}_{-0.08}$	1.50	$0.39^{+0.16}_{-0.13}$	19
XXL disturbed FS	$13.62^{+0.05}_{-0.12}$	1.50	$0.75^{+0.31}_{-0.16}$	19

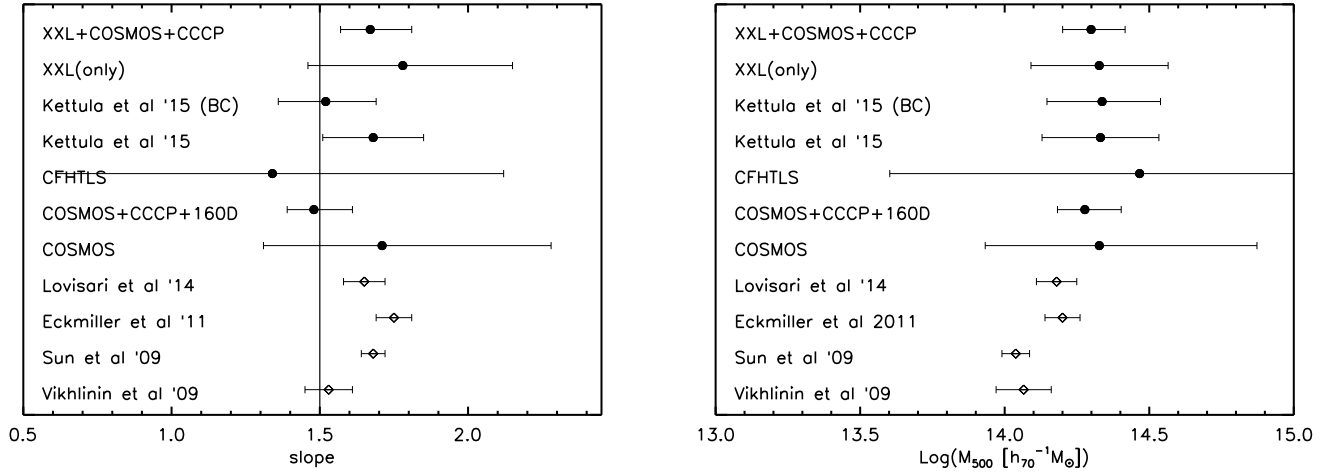


Fig. 8. LEFT: Comparison of our results on the slope of the mass-temperature relation with those in the literature (Eckmiller et al. 2011; Lovisari et al. 2015; Sun et al. 2009; Vikhlinin et al. 2009). RIGHT: Comparison of the mass of a cluster of temperature $T = 3$ keV at $z = 0.3$ based on mass-temperature relations and those in the literature. In both panels, filled circles are samples that use weak-lensing masses, open diamonds are samples that use hydrostatic masses. The COSMOS+CCCP+160D and COSMOS-only relations are from Kettula et al. (2013) and the CFHTLS relation from Kettula et al. (2015). BC has been corrected for Eddington bias.

4. Discussion

In §4.1 we discuss the effect of systematic uncertainties on our results, and in §4.2 we compare our results with the literature.

4.1. Systematic uncertainties

Several sources of systematic uncertainty have been discussed in the preceding sections. Here we describe the tests that were performed to assess the amplitude of these uncertainties.

Fitting method – We tested the robustness of the fitting method on the resultant scaling parameters using MPFITEXY (Williams et al. 2010). This is a variation of the standard IDL fitting technique MPFIT (Markwardt 2009) that minimises a χ^2 statistic and iteratively adjusts for intrinsic scatter. However, it does not calculate the error on the intrinsic scatter. Using MPFITEXY the XXL+COSMOS+CCCP fit of 96 objects produces a

slope of $b = 1.71 \pm 0.11$, intercept of $a = 13.55 \pm 0.09$, and intrinsic scatter of $\sigma_{\text{int ln } M/T} = 0.38$, i.e. fully consistent with our results presented in section 3 (Table 2).

Upper limits – To test the sensitivity of our results to the treatment of clusters with upper limits on $M_{500, \text{WL}}$ we re-fitted the mass-temperature relation excluding these objects, obtaining a marginally shallower slope of $b = 1.63 \pm 0.13$ and an intrinsic scatter of $\sigma_{\text{ln } M/T} = 0.39 \pm 0.06$ for the joint XXL+CCCP+COSMOS sample and $b = 1.84 \pm 0.38$, $\sigma_{\text{ln } M/T} = 0.30 \pm 0.18$ for the XXL-only sample – again, consistent with our main results.

Centring of the shear profile – Cluster masses are dominated by statistical noise such that whether we centre the shear profile on the BCG or on the X-ray centroid does not lead to a large systematic uncertainty. There is large scatter between the masses derived from the different centres; however, the bias is minimal

$\langle \langle M_{500,\text{WL}}^{\text{Xray}} / M_{500,\text{WL}}^{\text{BCG}} \rangle \rangle = 1.00 \pm 0.16$) and so does not have an impact on our results. The BCG centred fits return a XXL-CCCP-COSMOS combined MT relation with slope $b = 1.61 \pm 0.14$ and an intrinsic scatter of $\sigma_{\text{int,ln } M/T} = 0.43 \pm 0.06$.

Source selection – The photometric redshift uncertainty of galaxies and its contribution to the mass estimation of clusters in our sample is small $\langle d\xi/\xi \rangle = 0.13$ and so we used all background galaxies with $P(z)$ measurements that satisfy our redshift cuts (Section 2.4). Benjamin et al. (2013) use tests with spectroscopic redshifts to find that within the CFHTLenS catalogue the redshifts are most reliable between $0.1 < z < 1.3$. This is due to a fundamental degeneracy in the angular cross-correlation method. At $z < 0.1$, their contamination model tends to underpredict contamination by higher redshift galaxies. At $z > 1.3$ the predicted contamination by lower redshift galaxies is also underestimated. We compared masses derived using all galaxies to masses restricted to the reliable redshift range $0.1 < z < 1.3$. The masses are impervious to the two source selections with a ratio of $\langle M_{500,\text{WL}}^{0.1 < z < 1.3} / M_{500,\text{WL}} \rangle = 1.13 \pm 0.18$. In our sample only 10% of the systems include the $z < 0.1$ contaminated galaxies and the low number of $z > 1.3$ galaxies should contribute little to the shear. This in combination with the large statistical uncertainties on shear would explain the agreement.

Outer fitting radius – The systems considered in this article are lower mass than most of those considered by Becker & Kravtsov (2011). Thus the outer radius to which the NFW model is fitted to the measured shear profile may extend further into the infall region than in their simulation study, and thus might bias our mass measurements. We implemented a simple test whereby we compared the mass obtained from NFW models fitted to the annulus 0.15 – 2 Mpc to those described in section 2.4. The mean ratio of the masses derived from these fits and those upon which our results are based (0.15 – 3 Mpc) is 1.01 ± 0.17 .

Choice of mass-concentration relation – We adopted the Duffy et al. (2008) mass-concentration relation for our mass modelling of the shear signal, which aids comparison with the literature (Kettula et al. 2013). However observational studies (e.g. Okabe et al. 2013; Umetsu et al. 2014) indicate that clusters are more concentrated than expected from simulations (e.g. Duffy et al. 2008; Bhattacharya et al. 2013). Hoekstra et al. (2012) show that a 20% change in normalisation of the mass-concentration relation would bias NFW-based masses by $\sim 5 - 15\%$, although recent work by Sereno et al. (2015) suggest the bias could be accounted for by selection effects. As a simple test, we perturbed the normalisation of the Duffy et al. (2008) relation by a factor of 1.31 to bring it into line with the stacked weak-lensing analysis of Okabe et al. (2013). The masses that we computed using this perturbed relation are slightly lower than our Duffy-based masses, although consistent within the errors: $\langle M_{\text{Perturbed}} / M_{\text{Duffy}} \rangle = 0.93 \pm 0.14$. Although it is possible to obtain a mass when allowing concentration to be a free parameter ($\langle M_{\text{free}} / M_{\text{Duffy}} \rangle = 0.87 \pm 0.14$), we did not do this as we were not able to constrain concentration with this data. The slope of the mass-temperature relation fits to the joint sample, based on our perturbed and free-concentration masses are $b_{\text{perturbed}} = 1.75 \pm 0.13$ and $b_{\text{free}} = 1.71 \pm 0.14$. Within the errors both are consistent with the Duffy concentration prior results. The XXL-only M–T relation using free-concentration masses has regression parameters $b = 1.77 \pm 0.37$, $a = 13.54 \pm 0.21$, and $\sigma_{\text{ln } M/T} = 0.38 \pm 0.20$.

Cosmic shear test – Heymans et al. (2012) compute the star-galaxy cross-correlation function of objects within the

CFHTLenS catalogue finding an amplitude much higher than expected from simulations. Approximately 25% the fields fail this cosmic shear test and when rejected bring the observations back into agreement with simulations. This affects $\sim 40\%$ of our systems: XLSSC 054, 055, 060, 056, 091, 095, 096, 098, 099, 103, 104, 105, 107, 108, 110, and 111. Excluding these systems from our sample does not significantly change our results; for example a joint fit to the remaining XXL clusters, COSMOS, and CCCP (80 systems in total) yields $a = 13.43^{+0.13}_{-0.09}$, $b = 1.79^{+0.16}_{-0.12}$, $\sigma_{\text{int,ln } M/T} = 0.42^{+0.07}_{-0.06}$. This suggests that it has an insignificant effect on cluster lensing where PSF residuals are reduced from the radial averaging. All CFHTLenS fields are used in both Velander et al. (2014) and Kettula et al. (2015).

Mismatch in temperature measurement apertures – As discussed in the results section, our temperature measurement aperture differs from that used by CCCP. This should not dramatically affect our results as the temperature profile of clusters is shallow and for groups 0.3 Mpc is a significant fraction of $r_{500,\text{WL}}$, whereas for the massive clusters in CCCP the same holds at 0.5 Mpc. Nonetheless, as a test we computed temperatures within the same 0.5 Mpc aperture for our clusters, finding that this measurement is feasible for 36 of the 38 XXL clusters, and for all 10 COSMOS groups. The best fit slope parameter and intrinsic scatter for this fully self-consistent non-core excised relation are $b = 1.61 \pm 0.12$, and $\sigma_{(\text{ln } M/T)} = 0.42 \pm 0.06$. The mismatched aperture uncertainty is therefore comparable to the statistical errors, and does not alter our result.

Selection function – The XXL-100-GC sample selection function needs to account for the flux-limit, survey volume, pointings and more. In the M–T relation this calculation is not trivial. We created a simplified toy model to test the bias in measured slope on a flux limited sample as a function of the correlation between X-ray luminosity and temperature. For this test we took a population of 10,000 groups and clusters with masses ($1 \times 10^{13} < M_{500} < 1 \times 10^{15} M_{\odot}$) and redshifts ($0 < z < 1.5$) from the Tinker et al. (2008) mass function. We converted the mass simultaneously to X-ray luminosity using the scaling relation in Maughan (2014) and temperature using a relation of slope 1.5, normalisation 13.65. These were drawn from a bivariate Gaussian distribution with intrinsic scatter in \log_{10} of 0.4 and 0.3 for luminosity and temperature, respectively, and repeated for correlation coefficients between luminosity and temperature from 0 to 1 in steps of 0.05. Each luminosity was then converted to a flux and a cut at $3 \times 10^{-14} \text{ ergs s}^{-1} \text{ cm}^{-2}$ was applied to replicate the selection on the XXL-100-GC sample. We drew 20 samples of 100 clusters before and after the flux cut for each of the correlation coefficients between L–T and fitted the mass-temperature relation for each of these samples. Comparing the bias between the scaling relation parameters measured before and after the flux cut as a function of the correlation between L–T shows a weak dependency. We expect the correlation coefficient between luminosity and temperature to be ~ 0.3 (e.g. Maughan 2014). In our model this corresponds to less than 5% bias in both slope and normalisation. Kettula et al. (2015) apply a correction for Eddington bias to both masses and temperatures to a sample similar to ours in their scaling relation. Their results indicate a 10% bias on the slope when uncorrected for; however, this is detected at 0.7σ significance. For the CCCP clusters used in this paper, a selection function model is not possible. The CCCP sample is selected from a variety of archived data and various selection criteria. We note that the selection function test above only applies to the XXL-only sample, but will

be modelled comprehensively in a future XXL paper, when an alternative massive cluster sample with a well-defined selection function is available.

Outliers – One particular outlier in our sample is XLSSC 110. This system has been studied in detail by Verdugo et al. (2011) and is particularly interesting for the strong lensing features caused by a merger of three galaxies. For this system the temperature is particularly low for the estimated mass. If we instead centre our shear profiles on the merger (corresponding to the BCG) we obtain a 25% higher mass. For this system the temperature may have been underestimated by the exclusion of the AGN contaminated emission from the merger. Verdugo et al. (2011) use several methods to estimate the mass of this system but within a fixed radius. Refitting the joint scaling relation excluding this system gives constraints of $b = 1.71 \pm 0.13$, $a = 13.54 \pm 0.09$, and $\sigma_{\ln M/T} = 0.41 \pm 0.06$.

Mass bias on XXL-100-GC masses – To test the impact of biases on the individually measured weak-lensing masses in the XXL sample on the masses derived from the $M-T$ relation, we perturbed the XXL masses down by increments of 10%, refitted the joint $M-T$ relation, and recomputed the masses of XXL-100-GC. We find for offsets of 10, 20, and 30% in XXL masses, the resulting $M-T$ derived masses, $M_{500,MT}$, will be lower by 0.04 ± 0.02 , 0.10 ± 0.06 , and 0.22 ± 0.08 , respectively. Hence the systematics discussed in this section will have a relatively small influence on the XXL-100-GC masses computed from the $M-T$ relation given the large uncertainties on the linear regression parameters and temperature.

4.2. Comparison with the literature

The mass-temperature relation fitted to the 96 clusters and groups spanning $T \simeq 1 - 10$ keV from XXL, COSMOS, and CCCP has a slope of $b = 1.67^{+0.14}_{-0.10}$. This is 1.5σ higher than the self-similar prediction (Kaiser 1986). Most previous weak-lensing based measurements of this relation have concentrated on higher redshift samples, and/or a smaller (higher) temperature range (Smith et al. 2005; Bardeau et al. 2007; Hoekstra 2007; Okabe et al. 2010; Jee et al. 2011; Mahdavi et al. 2013), thus precluding useful comparison with our joint study of groups and clusters. Our slope is marginally steeper (1.1σ significance) than the most comparable study, that of Kettula et al. (2013), who obtained a slope of $b = 1.48^{+0.13}_{-0.09}$ for a sample of 65 groups and clusters spanning a similar temperature and redshift range to ours. The main difference between their study and ours is that ours includes 38 new systems from XXL-100-GC, we use the latest CCCP masses and the temperatures are measured in different ways. We measure temperatures within a fixed metric aperture of 300 kpc, whereas Kettula et al. measure temperatures within an annulus that excludes the core and scales with the mass of the cluster, $0.1r_{500,WL} < R < 0.5r_{500,WL}$. Nevertheless, within the current statistical precision the intercept and slope of the respective relations agree (Figure 8). We also note that the predicted self-similar slope applies to relations based on core-excised temperature measurements. We also express the normalisation of these two relations and those of others from the literature as the mass of a cluster at $z = 0.3$ with a temperature of $T = 3$ keV to facilitate comparison between relations that differ in the details of how they are defined. We see that the relations based on weak-lensing calibrated mass in the group regime favour $\sim 40\%$ higher normalisations than hydrostatic relations at $\sim 1 - 2\sigma$. Although the bias correction applied by Kettula et al. (2015) can reproduce the self-similar slope, it has a negligible

effect on the mass estimated at fixed $T = 3$ keV and $z = 0.3$ (Figure 8)

Two of our clusters (XLSSC 091 and XLSSC 006) also appear in Kettula et al. (2015) under their XID 111180 and 102760, using the same CFHTLenS survey data. The former has a spectroscopic redshift of 0.185 (Mirkazemi et al. 2015), whereas the latter has a photometric measurement of 0.47 (Gozaliasl et al. 2014), compared to our values of 0.186 and 0.429. For XLSSC 091 and XLSSC 006 respectively, the right ascension and declination are measured in XXL to be 37.926, -4.881 and 35.438, -3.772, whereas they appear in table 1 of Kettula et al. (2015) at 37.9269, -4.8814 and 35.4391, -3.7712. The respective offsets are $\sim 3.5''$ and $\sim 4.9''$. They measure masses $M_{500,WL} = 8.5 \pm 2.1 \times 10^{14} h_{70}^{-1} M_{\odot}$ and $5.5 \pm 3.3 \times 10^{14} h_{70}^{-1} M_{\odot}$ and temperatures of $T = 5 \pm 0.6$ keV and 8.2 ± 5.6 keV. These agree with our masses and temperatures within the statistical errors.

Most studies of the mass-temperature relation of groups and clusters have relied on X-ray data to estimate mass, and thus assumed that the intracluster medium is in hydrostatic equilibrium (e.g. Finoguenov et al. 2001; Sun et al. 2009; Eckmiller et al. 2011; Lovisari et al. 2015). These authors obtained slopes of $b \simeq 1.65 - 1.75$ with a statistical uncertainty of ~ 0.05 . The Kettula et al. core-excised weak-lensing relation is in tension with the hydrostatic results at the $1-2\sigma$ level suggesting that the difference between the lensing and X-ray based mass-temperature relations is mass dependent. The slope of our weak-lensing-based non-core excised mass-temperature relation is, however, in agreement with the slope of the hydrostatic mass-temperature relations.

Several observational and theoretical studies have found that hydrostatic equilibrium may not be a valid assumption in the most massive clusters (e.g. Nagai et al. 2007; Mahdavi et al. 2008, 2013; Shaw et al. 2010; Zhang et al. 2010; Rasia et al. 2012; Israel et al. 2015). The assumption of hydrostatic equilibrium has not yet been explored in great detail in galaxy groups, i.e. $T \lesssim 3$ keV; however, Borgani et al. (2004) pointed out that the steep slope of the hydrostatic mass-temperature relation of groups is hard to reproduce with simulations. More recent papers of Le Brun et al. (2014); Pike et al. (2014); Planelles et al. (2014) show that the reproducibility of scaling relations is dependent on the physics included in the simulation. Simulations including baryonic processes are expected to bias scaling relations from the self-similar prediction with a stronger effect on low-mass systems where the baryons are more important. The statistical precision of our results is not sufficient to test whether the validity of hydrostatic equilibrium is a function of halo mass.

5. Summary

We have presented a study of the mass-temperature relation of galaxy groups and clusters spanning $T \simeq 1 - 10$ keV, based on weak-lensing mass measurements. Our main analysis is based on the 38 systems drawn from the XXL 100 brightest cluster sample, that also lie within the footprint of the CFHTLenS shear catalog. Here we summarise the main results of this paper:

- We measured individual weak-lensing masses of clusters within XXL-100-GC with careful checks on systematics. In this mass ($M_{500} \sim 10^{13} - 10^{15} M_{\odot}$) and temperature range ($1 \lesssim T \lesssim 6$ keV) this is currently the largest sample of groups and poor clusters with weak-lensing masses available for studying the mass-temperature relation.

- We used the masses to calibrate the mass-temperature relation down to the group and poor cluster mass scale. This relation has a slope of $1.78^{+0.37}_{-0.32}$.
- We find that the scatter in our XXL-only mass-temperature relation is dominated by systems with significant offsets between their BCG and X-ray centroids. This suggests that ongoing/recent merging activity may act to increase the scatter by affecting the accuracy of our weak-lensing mass measurements and/or by perturbing the temperature of the merging systems. We will return to this issue when better quality data become available.
- We increased the sample by incorporating 48 massive clusters from CCCP and 10 X-ray selected groups from COSMOS. This extended sample spans the temperature range $T \approx 1 - 10$ keV. The mass-temperature relation for this extended sample is steeper than the self-similar prediction, with a slope of $1.67^{+0.14}_{-0.10}$ and intrinsic scatter of $\sigma_{\ln M|T} = 0.41$. We used this relation to estimate the mass of each member of XXL-100-GC; these masses are available in Paper III.
- The slope of our mass-temperature relation is in agreement with relations based on assuming hydrostatic equilibrium favouring a steeper slope than self-similar. Whilst insignificant given the current uncertainties, this result is in tension with previous weak-lensing studies that suggest non-thermal pressure support being more significant in lower mass systems. However, the offset in the normalisation of the relations estimated by comparing the mass of a 3 keV system at $z = 0.3$ using the available relations implies that the hydrostatic mass of a 3 keV system is $\sim 40\%$ lower than that obtained using a weak-lensing mass-temperature relation, which may indicate a halo mass dependent hydrostatic mass bias.

Our future programme will extend mass-observable scaling relations for groups and clusters in the XXL and related surveys to include other mass proxies, including gas mass and K -band luminosity. We will also expand the sample of groups and poor clusters available for this work as deeper weak-lensing data becomes available for XXL-N from Hyper Suprime-CAM, and high-quality weak-lensing data become available for XXL-S from our ongoing observations with Omegacam on the ESO VLT Survey Telescope. These enlarged samples and the improved statistical precision will also motivate careful modelling and the incorporation of the selection function into our analysis.

Acknowledgements. This work is based on observations obtained with MegaPrime/MegaCam, a joint project of CFHT and CEA/DAPNIA, at the Canada-France-Hawaii Telescope (CFHT), which is operated by the National Research Council (NRC) of Canada, the Institut National des Sciences de l'Univers of the Centre National de la Recherche Scientifique (CNRS) of France, and the University of Hawaii. This research used the facilities of the Canadian Astronomy Data Centre operated by the National Research Council of Canada with the support of the Canadian Space Agency. CFHTLenS data processing was made possible thanks to significant computing support from the NSERC Research Tools and Instruments grant program.

We thank the anonymous referee for useful comments and Doug Applegate, Mark Birkinshaw, Gus Evrard, Will Farr, Catherine Heymans, Henk Hoekstra, Kimo Kettula, Sarah Mulroy, Nobuhiro Okabe, Thomas Reiprich, Tim Schrabback, Mauro Sereno and Trevor Sidery for helpful discussions and assistance. ML acknowledges a Postgraduate Studentship from the Science and Technology Facilities Council. GPS acknowledges support from the Royal Society. FP acknowledges support from the BMBF/DLR grant 50 OR 1117, the DFG grant RE 1462-6 and the DFG Transregio Programme TR33. GPS, FZ, TJP, BM, PG acknowledge support from the Science and Technology Facilities Council.

References

- Bahé, Y. M., McCarthy, I. G., & King, L. J. 2012, MNRAS, 421, 1073
 Bardeau, S., Soucail, G., Kneib, J.-P., et al. 2007, A&A, 470, 449
 Becker, M. R., & Kravtsov, A. V. 2011, ApJ, 740, 25
 Benjamin, J., Van Waerbeke, L., Heymans, C., et al. 2013, MNRAS, 431, 1547
 Bhattacharya, S., Habib, S., Heitmann, K., & Vikhlinin, A. 2013, ApJ, 766, 32
 Böhringer, H., Dolag, K., & Chon, G. 2012, A&A, 539, A120
 Borgani, S., Murante, G., Springel, V., et al. 2004, MNRAS, 348, 1078
 Clerc, N., Adami, C., Lieu, M., et al. 2014, MNRAS, 444, 2723
 Connor, T., Donahue, M., Sun, M., et al. 2014, ApJ, 794, 48
 Corless, V. L., & King, L. J. 2007, MNRAS, 380, 149
 Duffy, A. R., Schaye, J., Kay, S. T., & Dalla Vecchia, C. 2008, MNRAS, 390, L64
 Démoclès, J., et al., in prep.
 Eckmiller, H. J., Hudson, D. S., & Reiprich, T. H. 2011, A&A, 535, A105
 Erben, T., Hildebrandt, H., Miller, L., et al. 2013, MNRAS, 433, 2545
 Evrard, A. E., MacFarland, T. J., Couchman, H. M. P., et al. 2002, ApJ, 573, 7
 Finoguenov, A., Reiprich, T. H., Böhringer, H. 2001, A&A, 368, 749
 Gelman, A., Rubin D. 1992. Inference from Iterative Simulation Using Multiple Sequences. *Statistical Science*, 7, 457–511.
 Giles, P. A., Maughan, B. J., Pacaud, P., et al. 2016, A&A, submitted (XXL Survey, III)
 Giodini, S., Lovisari, L., Pointecouteau, E., et al. 2013, Space Sci. Rev., 177, 247
 Gozaliasl, G., Finoguenov, A., Khosroshahi, H. G., et al. 2014, A&A, 566, A140
 Heymans, C., Van Waerbeke, L., Miller, L., et al. 2012, MNRAS, 427, 146
 Hildebrandt, H., Erben, T., Kuijken, K., et al. 2012, MNRAS, 421, 2355
 Hinshaw, G., Larson, D., Komatsu, E., et al. 2013, ApJS, 208, 19
 Hoekstra, H. 2007, MNRAS, 379, 317
 Hoekstra, H., Mahdavi, A., Babul, A., & Bildfell, C. 2012, MNRAS, 427, 1298
 Hoekstra, H., Herbonnet, R., Muzzin, A., et al. 2015, MNRAS, 449, 685
 Israel, H., Schellenberger, G., Nevalainen, J., Massey, R., & Reiprich, T. H. 2015, MNRAS, 448, 814
 Jee, M. J., Dawson, K. S., Hoekstra, H., et al. 2011, ApJ, 737, 59
 Kaiser, N. 1986, MNRAS, 222, 323
 Kelly, B. C. 2007, ApJ, 665, 1489
 Kettula, K., Finoguenov, A., Massey, R., et al. 2013, ApJ, 778, 74
 Kettula, K., Giodini, S., van Uitert, E., et al. 2015, MNRAS, 451, 1460
 Lavoie, S., et al., in prep.
 Le Brun, A. M. C., McCarthy, I. G., Schaye, J., & Ponman, T. J. 2014, MNRAS, 441, 1270
 Leauthaud, A., Finoguenov, A., Kneib, J.-P., et al. 2010, ApJ, 709, 97
 Lovisari, L., Reiprich, T. H., & Schellenberger, G. 2015, A&A, 573, A118
 Maughan, B. J. 2014, MNRAS, 437, 1171
 Mahdavi, A., Hoekstra, H., Babul, A., & Henry, J. P. 2008, MNRAS, 384, 1567
 Mahdavi, A., Hoekstra, H., Babul, A., et al. 2013, ApJ, 767, 116
 Markwardt, C. B. 2009, *Astronomical Data Analysis Software and Systems XVIII*, 411, 251
 Meneghetti, M., Rasia, E., Merten, J., et al. 2010, A&A, 514, AA93
 Miller, L., Heymans, C., Kitching, T. D., et al. 2013, MNRAS, 429, 2858
 Mirkazemi, M., Finoguenov, A., Pereira, M. J., et al. 2015, ApJ, 799, 60
 Nagai, D., Vikhlinin, A., & Kravtsov, A. V. 2007, ApJ, 655, 98
 Navarro, J. F., Frenk, C. S., & White, S. D. M. 1997, ApJ, 490, 493
 Okabe, N., Takada, M., Umetsu, K., Futamase, T., & Smith, G. P. 2010, PASJ, 62, 811
 Okabe, N., Smith, G. P., Umetsu, K., Takada, M., & Futamase, T. 2013, ApJ, 769, L35
 Pacaud, F., Clerc, N., Giles, P. A., et al. 2016, A&A, submitted (XXL Survey, II)
 Pierre, M., Valtchanov, I., Altieri, B., et al. 2004, *J. Cosmology Astropart. Phys.*, 9, 011
 Pierre, M., Pacaud, F., Adami, C., et al. 2016, A&A, submitted (XXL Survey, I)
 Pike, S. R., Kay, S. T., Newton, R. D. A., Thomas, P. A., & Jenkins, A. 2014, MNRAS, 445, 1774
 Planelles, S., Borgani, S., Fabjan, D., et al. 2014, MNRAS, 438, 195
 Rasia, E., Meneghetti, M., Martino, R., et al. 2012, *New Journal of Physics*, 14, 055018
 Santos, J. S., Rosati, P., Tozzi, P., et al. 2008, A&A, 483, 35
 Schneider, P., van Waerbeke, L., Jain, B., & Kruse, G. 1998, MNRAS, 296, 873
 Sereno, M., Giocoli, C., Ettori, S., & Moscardini, L. 2015, MNRAS, 449, 2024
 Shaw, L. D., Nagai, D., Bhattacharya, S., & Lau, E. T. 2010, ApJ, 725, 1452
 Smith, G. P., Kneib, J.-P., Smail, I., et al. 2005, MNRAS, 359, 417
 Šuhada, R., Song, J., Böhringer, H., et al. 2012, A&A, 537, AA39
 Sun, M., Voit, G. M., Donahue, M., et al. 2009, ApJ, 693, 1142
 Tinker, J., Kravtsov, A. V., Klypin, A., et al. 2008, ApJ, 688, 709
 Umetsu, K., Medezinski, E., Nonino, M., et al. 2014, ApJ, 795, 163
 Velander, M., van Uitert, E., Hoekstra, H., et al. 2014, MNRAS, 437, 2111
 Vikhlinin, A., Burenin, R. A., Ebeling, H., et al. 2009, ApJ, 692, 1033
 Williams, M. J., Bureau, M., & Cappellari, M. 2010, MNRAS, 409, 1330

- Verdugo, T., Motta, V., Muñoz, R. P., et al. 2011, *A&A*, 527, A124
Wright, C. O., & Brainerd, T. G. 2000, *ApJ*, 534, 34z
Zhang, Y.-Y., Okabe, N., Finoguenov, A., et al. 2010, *ApJ*, 711, 1033

Appendix A: Shear profiles

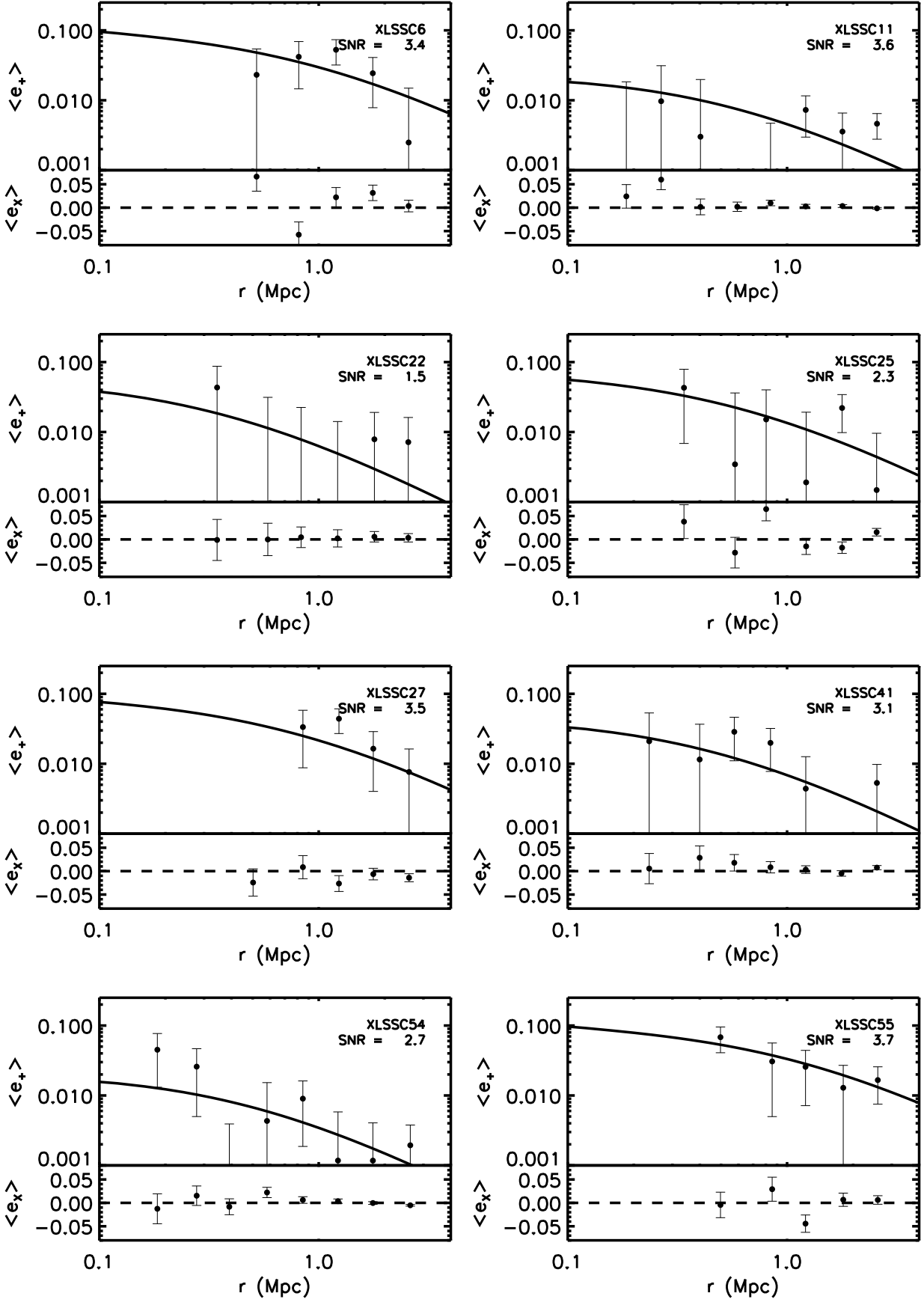


Fig. A.1. Tangential and cross-component ellipticity as a function of distance from cluster centre.

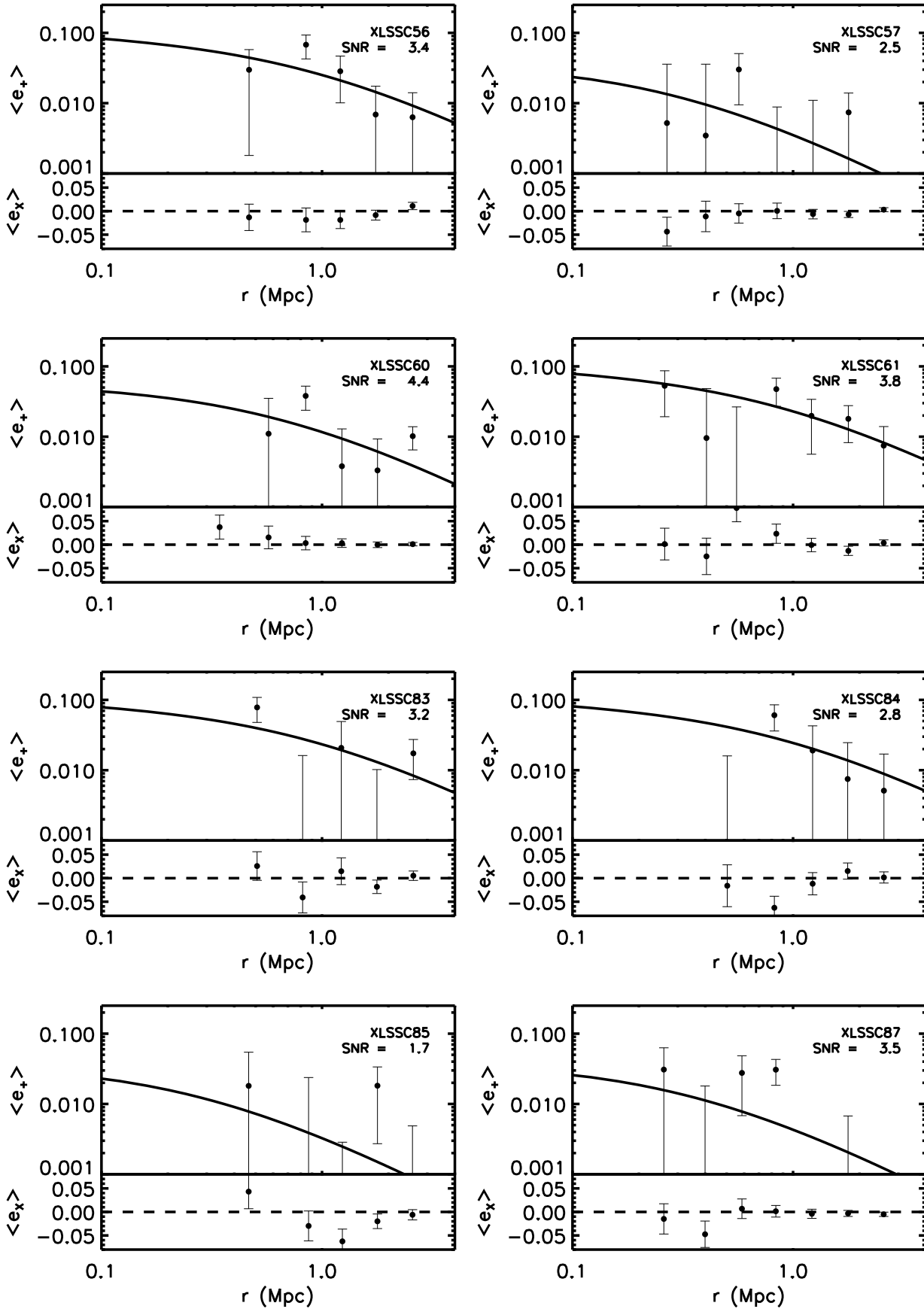


Fig. A.2. Tangential and cross-component ellipticity as a function of distance from cluster centre.

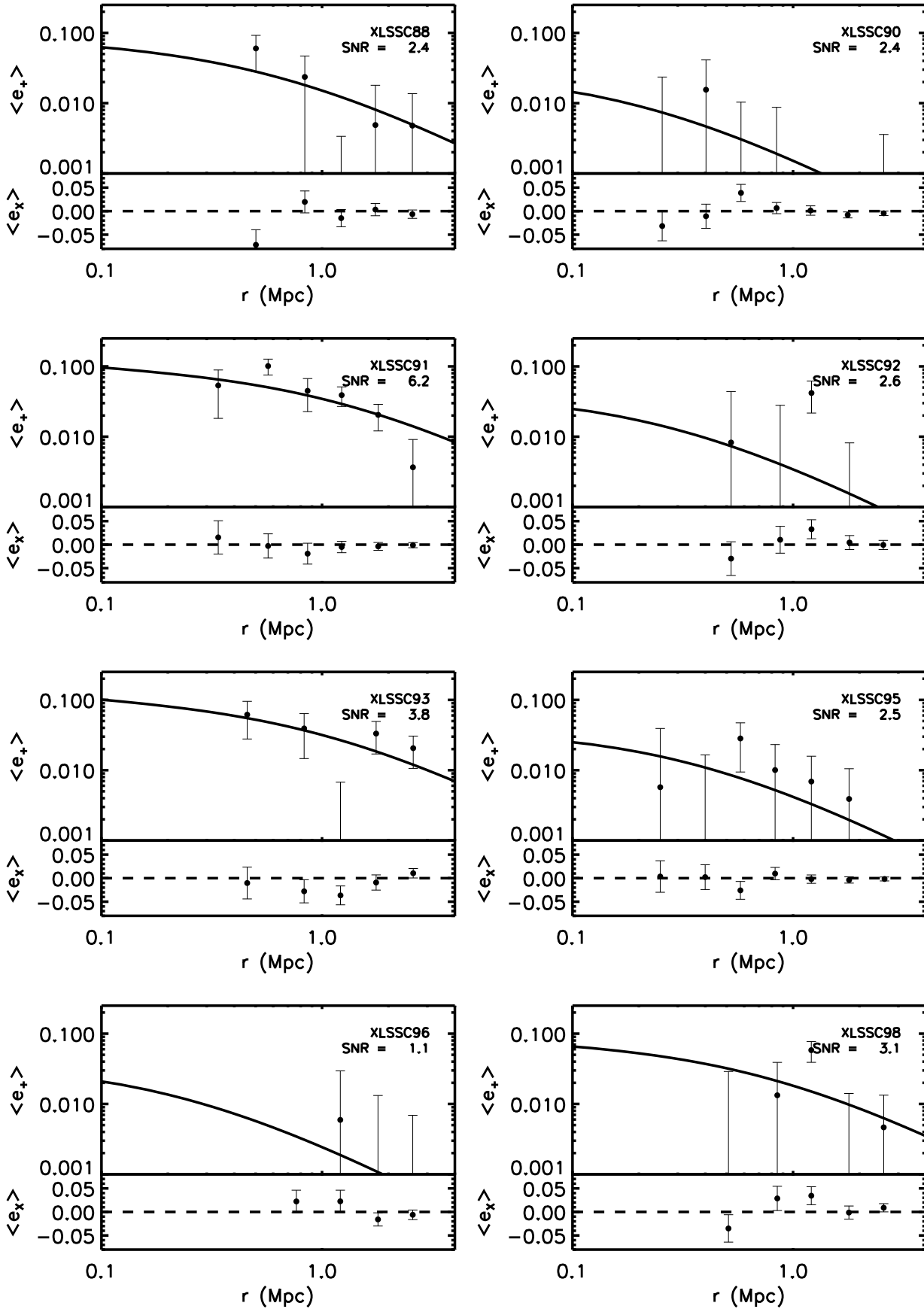


Fig. A.3. Tangential and cross-component ellipticity as a function of distance from cluster centre.

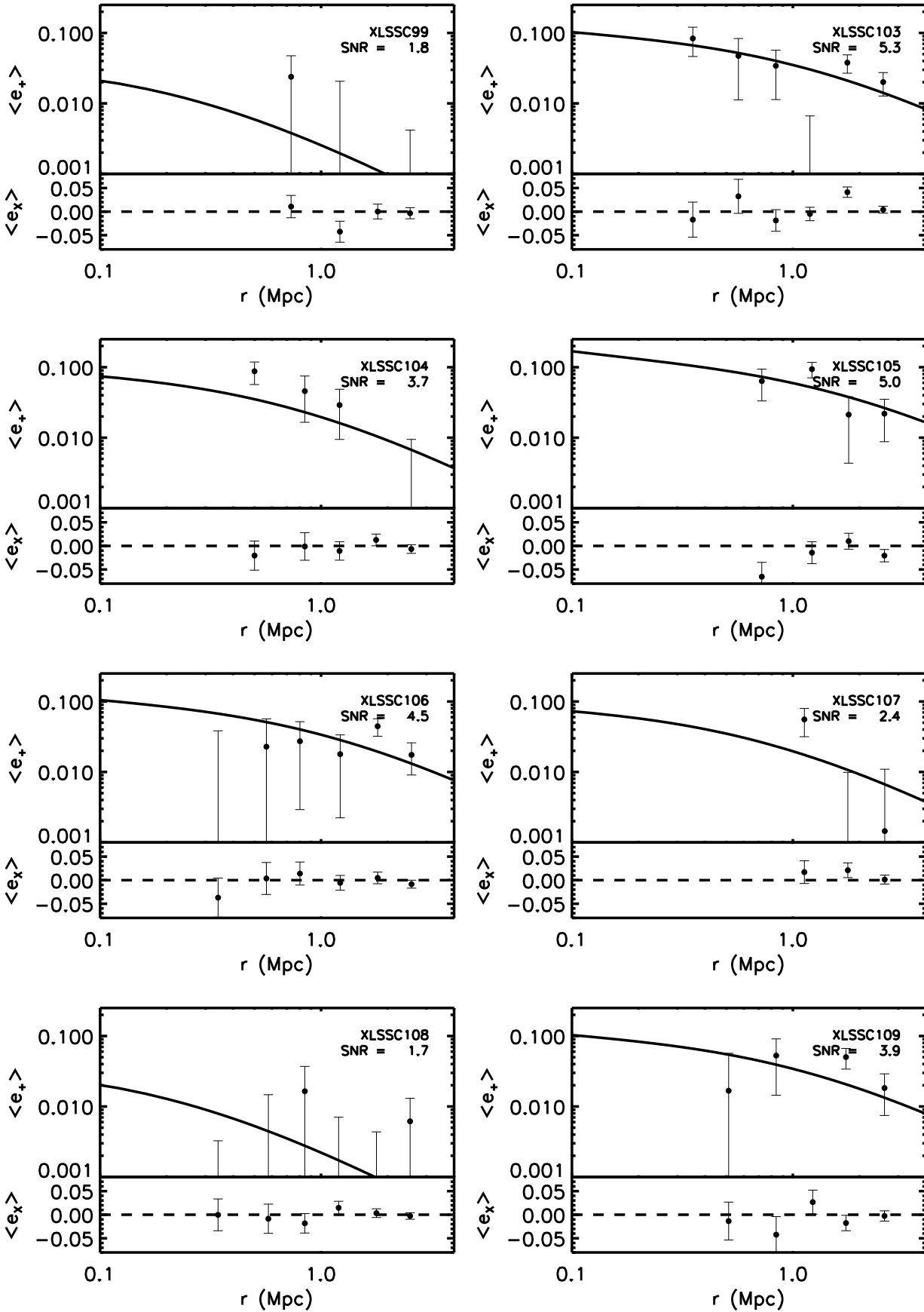


Fig. A.4. Tangential and cross-component ellipticity as a function of distance from cluster centre.

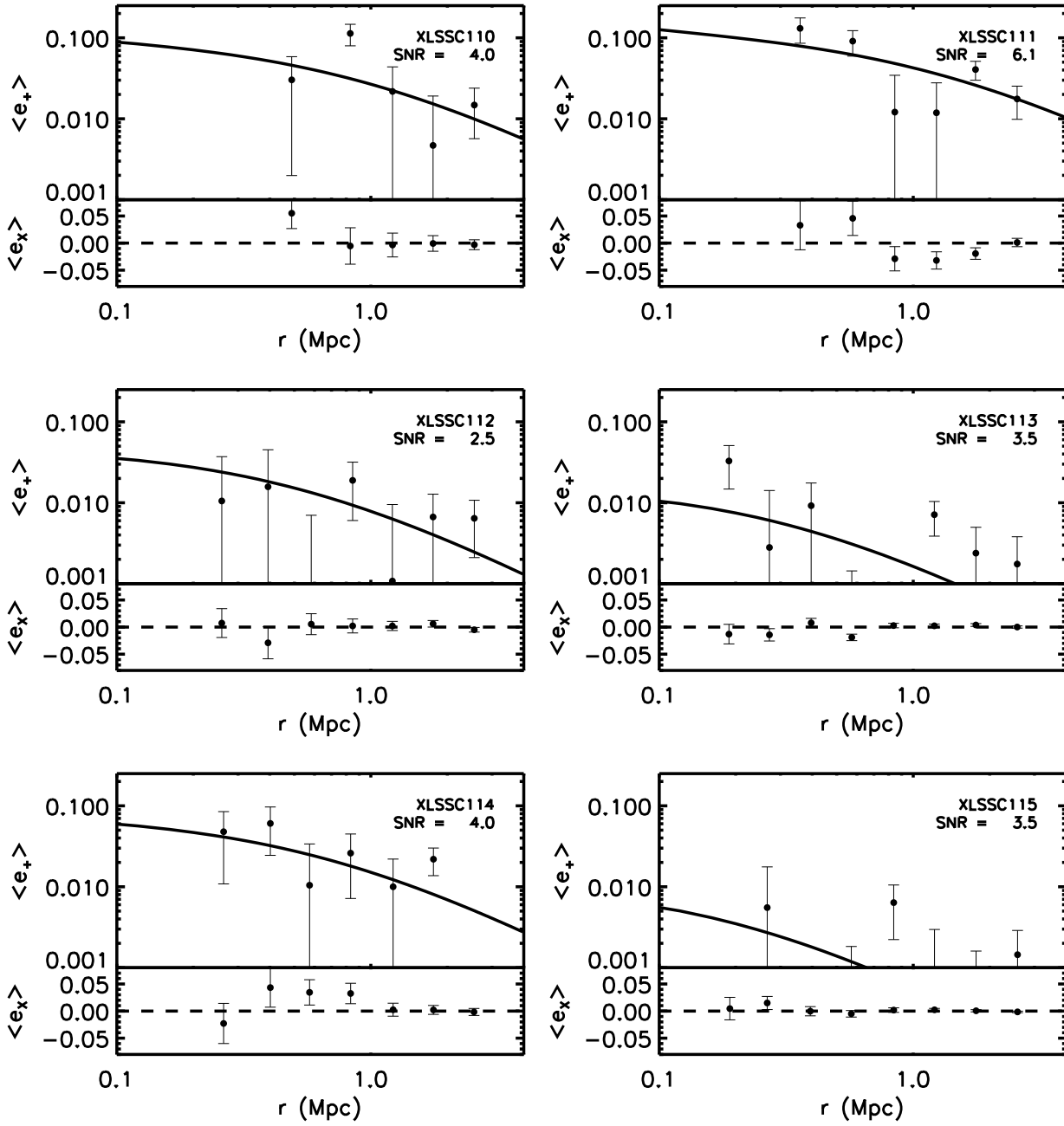


Fig. A.5. Tangential and cross component ellipticity as a function of distance from cluster centre.